BRNO UNIVERSITY OF TECHNOLOGY

VYSOKÉ UČENÍ TECHNICKÉ V BRNĚ

FACULTY OF CHEMISTRY

FAKULTA CHEMICKÁ

INSTITUTE OF MATERIALS SCIENCE

ÚSTAV CHEMIE MATERIÁLŮ

THE EFFECT OF MORPHOLOGY ON THE MECHANICAL PROPERTIES OF 3D PRINTED BONE SCAFFOLDS

VLIV MORFOLOGIE NA MECHANICKÉ VLASTNOSTI 3D TIŠTĚNÝCH KOSTNÍCH NOSIČŮ

MASTER'S THESIS

DIPLOMOVÁ PRÁCE

AUTHOR — **Bc. Martin Zetocha**

AUTOR PRÁCE

SUPERVISOR — **doc. Ing. Lucy Vojtová, Ph.D.**

VEDOUCÍ PRÁCE

BRNO 2022

BRNO UNIVERSITY OF TECHNOLOGY
FACULTY OF CHEMISTRY

Assignment Master's Thesis

Project no.:	FCH-DIP1762/2021	Academic year: 2021/22
Department:	Institute of Materials Science	
Student:	**Bc. Martin Zetocha**	
Study programme:	Chemistry, Technology and Properties of Materials	
Study field:	Chemistry, Technology and Properties of Materials	
Head of thesis:	**doc. Ing. Lucy Vojtová, Ph.D.**	

Title of Master's Thesis:

The effect of morphology on the mechanical properties of 3D printed bone scaffolds

Master's Thesis:

1) Literature search on the topic of extrusion 3D printing of cement scaffolds, various types of morphology, and their effect on the mechanical properties.
2) Preparation and characterization of 3D printed cement carriers with different morphology.
3) Measurement of mechanical properties of prepared samples.
4) Evaluation of results.
5) Conclusion.

Deadline for Master's Thesis delivery: 13.5.2022:

Master's Thesis should be submitted to the institute's secretariat in a number of copies as set by the dean This specification is part of Master's Thesis

Bc. Martin Zetocha student	doc. Ing. Lucy Vojtová, Ph.D. Head of thesis	doc. Ing. František Šoukal, Ph.D. Head of department

In Brno dated 1.2.2022

prof. Ing. Michal Veselý, CSc.
Dean

ABSTRACT

This diploma thesis deals with the study of the effect of morphology on the mechanical properties of 3D printed bone scaffolds. The theoretical part briefly summarized bone tissue engineering as well as possibilities to construct such scaffolds using 3D printing technologies. Further, it is focused on utilized materials and key architectural parameters in designing and producing 3D printed bone scaffolds. The experimental part deals with the optimization of 3D printing, including the determination of the most suitable shape. Later, designing custom infill structures that would be printable and practically usable are evaluated. Such designs were then subjected to mechanical testing to determine their strength, elastic gradient, and the energy they are able to absorb. In terms of mechanical properties, results from used infill structures showed that honeycomb iterations proved to be superior.

KEYWORDS

3D printing, bone cement, bone scaffold, infill structures, bone tissue engineering, mechanical properties, strength, elastic gradient, absorbed energy.

ABSTRAKT

Táto diplomová práca sa zaoberá štúdiom vplyvu morfológie na mechanické vlastnosti 3D tlačených kostných scaffoldov. Teoretická časť stručne zhrnula inžinierstvo kostného tkaniva a taktiež možnosti konštrukcie takýchto scaffoldov pomocou technológií 3D tlače. Ďalej sa zamerala na použité materiály a kľúčové architektonické parametre pri navrhovaní a výrobe 3D tlačených kostných scaffoldov. Experimentálna časť sa najprv zaoberala optimalizáciou 3D tlače vrátane určenia najvhodnejšieho tvaru. Neskôr sa zamerala na navrhovanie vlastných vnútorných štruktúr, ktoré by boli tlačiteľné a prakticky použiteľné. Takéto konštrukcie boli potom podrobené mechanickému testovaniu, aby sa určila ich pevnosť, elastický gradient a energia, ktorú sú schopné absorbovať. Výsledky ukázali, že z použitých vnútorných štruktúr sú z hľadiska mechanických vlastností najlepšie iterácie šesťuholníkové alebo inač povedané honeycombu.

KLÚČOVÉ SLOVÁ

3D tlač, kostný cement, kostné skaffoldy, vnútorné štruktúry, inžinierstvo kostného tkaniva, mechanické vlastnosti, pevnosť, elastický gradient, absorbovaná energia.

CITATION

ZETOCHA, Martin. Vliv morfologie na mechanické vlastnosti 3D tištěných kostních nosičů. Brno, 2022. Dostupné také z: https://www.vutbr.cz/studenti/zav-prace/detail/140082. Diplomová práce. Vysoké učení technické v Brně, Fakulta chemická, Ústav chemie materiálů. Vedoucí práce Lucy Vojtová.

DECLARATION

I declare that the master's thesis has been worked out by myself and that all the quotations from the used literary sources are accurate and complete. The content of the master's thesis is the property of the Faculty of Chemistry of the Brno University of Technology, and all commercial uses are allowed only if approved by both the supervisor and the dean of the Faculty of Chemistry, BUT.

---

author's signature

Acknowledgement

I would like to thank my supervisor doc. Ing. Lucy Vojtová, Ph.D. for her time, expertise, and valuable advice. I would also like to thank my consultant Ing. Kristýna Hliháková for her unlimited patience, insight, help and encouragement. Further, I would like to thank Ing. Přemysl Menčík, Ph.D. for his expertise and 3D designs, Mgr. Jan Žídek, Ph.D. for his time and help with creation of infill designs, Ing. Radek Sedláček, Ph.D. and Ing. Martin Vltavský from the Czech technical university in Prague, Faculty of Mechanical Engineering for allowing me to test mechanical properties at their institute and their help with processing data, thanks to all my colleagues at the laboratory for their help and willingness especially to Bc. David Scholz for supplying XRD data and hints for 3D printing. I must especially thank my family for their support without which any of it would be possible and my girlfriend, who always knew I could do it. Lastly, I want to dedicate this work to my late friend Katarína Vicenová. May you rest in peace.

The proposed work was supported by the ProfiBONE project (TO01000309) benefits from a grant from Iceland, Liechtenstein, and Norway through the EEA Grants and the Technology Agency of the Czech Republic.

CONTENTS

INTRODUCTION

Functional disorders, defects and bone loss can be considered a long-term global health problem. Together with an aging world population, musculoskeletal conditions, and diseases such as fractures, osteoporosis, tumors, congenital defects, and many more are on the rise. In general, these health problems have significant impact on the quality of life of the ones affected by them, which calls for new innovative solutions [1, 2].

Currently, metal implants are the most common way to surgically treat fractures and joint arthroplasties. Nevertheless, implants like these are far from flawless and are subject to failures due to inflammation, osteolysis because of implant loosening, wear, and improper loading [3]. Among other treatments, autografts (bone implant from the patient's body) and allografts (bone implant from a donor) are considered golden standard, in bone grafting surgical procedures. But as even these methods face complications, synthetic bone grafts gradually attract more attention as possible solution, where such application of bone tissue engineering (BTS) can avoid problems connected with these treatments [4, 5].

Tissue engineering as well as bone tissue engineering combines advanced methods from material engineering and life sciences to create artificial constructs with the aim of regeneration of new tissue [6]. Mimicking the natural bone tissue its social for the design of artificial scaffolds compatible with BTE. Thus, the scaffold must possess mechanical properties similar to bone, as well as its bioactivity, biodegradability, and biocompatibility. The same importance should be dedicated to the architecture of the scaffold as porosity, pore size, and pore interconnection strongly influences not only its mechanical properties but cellular activity [7,8].

There are many ways to produce porous bone scaffolds, such as chemical/gas foaming, solvent casting, particle/salt leaching, freeze-drying, thermally induced phase separation, etc. However, these methods do not offer a reliable way to fabricate scaffolds with consistent aforementioned porous properties. That brings us to the use of additive manufacturing (AM). This method allows us to directly design and fabricate scaffolds with desired porous structure. For this thesis, the main focus will be pointed to the 3D printing of bone scaffolds. Since this approach is based on computer-aided design (CAD), it allows complex 3D structures tailored according to the individual patient's needs [5, 9].

1. THEORETICAL PART

1.1 Bone tissue engineering

1.1.1 Tissue engineering

Before focusing on bone tissue engineering, a short characterization of tissue engineering is required. Tissue engineering is a field connecting material and life sciences to solve medical problems like tissue loss and organ failure in clinical practice. Moreover, it can be defined as an "*attempt to harness the body's ability to regenerate damaged tissue by combining cells and bioactive factors in a biomaterial scaffold*" [10] (Sears, 2016). This approach typically combines biomaterial scaffolds with cells and bioactive factors, to fabricate implantable construct to replace or restore biological function. Ideally, the scaffold is resorbed, and functional tissue formation occurs [10].

In the last two decades, tissue engineering benefited from multiple advancements primarily from novel biomaterials, incorporation of nanotechnologies, stem cell technologies, 3D bioprinting technologies, etc. Thanks to these, promising developments were made in 3D tissue modeling for personalized tissue engineering therapies [11].

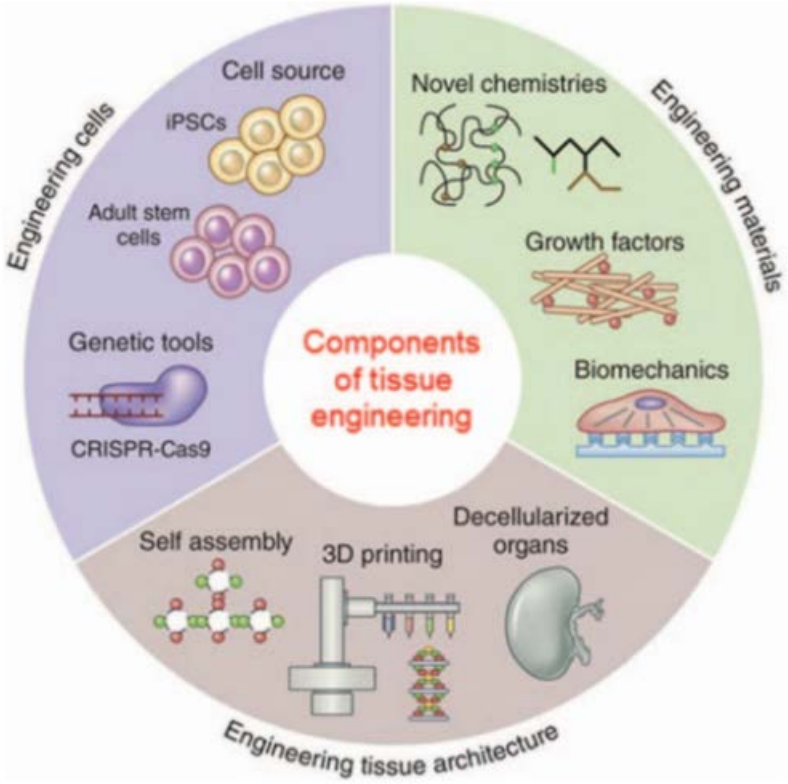

Fig. 1: *representation of different aspects of tissue engineering [12]*

1.1.2 Artificial bone grafts

Most orthopedic implants currently in use are still missing critical characteristics which

can be found in living tissue: (1) ability to self-repair; (2) ability to modify in response to external factors; (3) ability to sustain blood flow. As such properties for replacements are still impossible to achieve, the focus should transfer from replacement of tissues to regeneration of tissues [13].

An ideal scaffold for bone regeneration should adhere to certain requirements. Clinically viable scaffold should consider design and material properties which should be tailored for specific bone damage. The material needs to be biocompatible as not to provoke hostile physiological response of the host tissue. Furthermore, the scaffold should serve as a supporting structure while new tissue regenerates and degrades in tandem with regenerating tissue. Its architecture incorporates interconnected macro-porous network; bonds without development of scar tissue (osteoconductivity); promotes cell adhesion and absorption of metabolites; enables cell differentiation and proliferation; resorbs at an optimal rate and the degradation products can be excluded from the body. Technique used for processing should be able to produce irregular shapes to fit specific needs of the patient and exhibits sufficient mechanical properties to withstand in vivo conditions and handling during surgery procedures. In the end, however, the designed scaffold must be commercially lucrative [13,14].

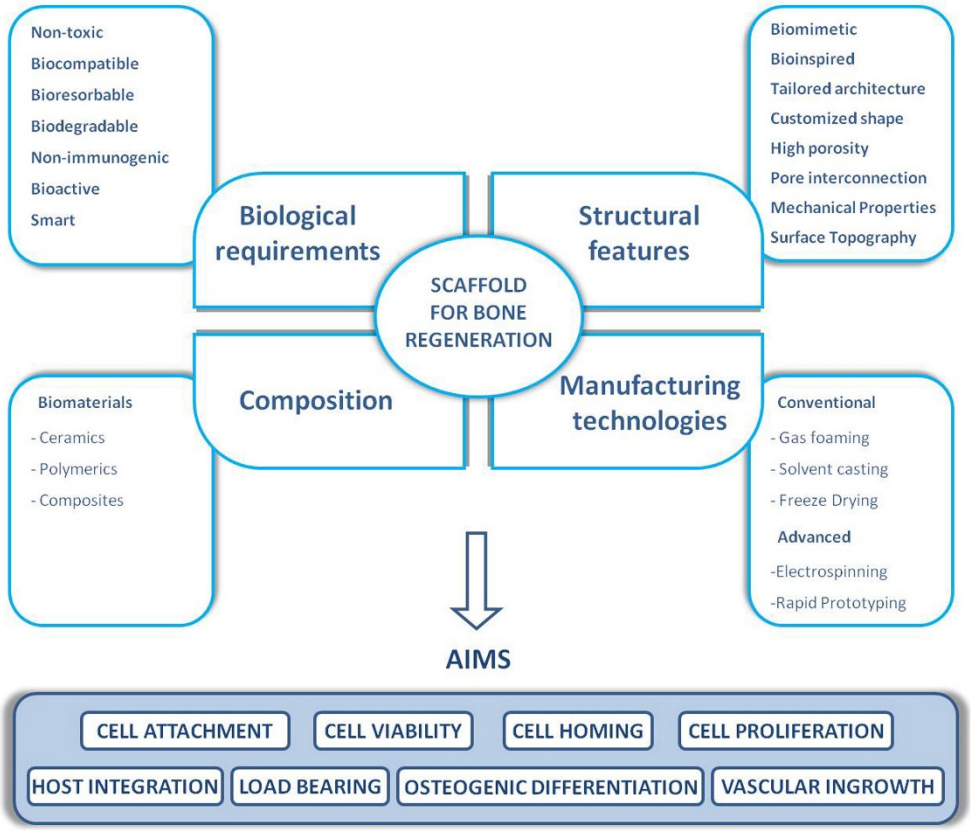

Fig. 2: *representation of different aspects applied in bone tissue engineering [15]*

1.1.3 Mechanical properties of bone

Even though bone is an organic material in many ways it acts the same way as artificial

engineering material. But unlike man-made materials, there are many factors that affect the mechanical properties of bone. Variations not only occur from patient to patient but are influenced by age and gender, the mineral content of the bone, location of the bone etc. To an extent these factors influence each other where for example mineral content of the bone changes with the age of the patient [16]. Bone matrix porosity and degree of mineralization play the primary role in the mechanical properties of bone.

Furthermore, bone as a material with an anisotropic structure proves its mechanical properties in two orthogonal directions: transverse and longitudinal. In the longitudinal direction, cortical bone is stronger if loaded along the diaphyseal axis and fracture toughness is super at the transverse direction [16, 17].

The bone structure mainly consists of collagen fibers and an inorganic matrix, resulting in a composite material.

Modulus

As such, its Young's modulus can be determined using the rule of mixture (1) and inverse rule of mixture (2).

$$(1)\ E_{ax} = f \cdot E_f + (1 - f) \cdot E_{m,}$$

$$(2)\ E_{ax} = \left[\frac{f}{E_f} + \frac{(1-f)}{E_m}\right]^{-1}$$

E_f, E_m stand for Young's Modulus of fibers and matrix and f stand for the volume fraction of fibers. The use of these formulas for the calculation of actual values for bone is feasible but the use of better approximations would be appropriate. For the purposes of this thesis, the further focus will be on actual values of young's modulus, density as the main function of young's modulus and compressive strength [16].

Table 1. *Young's modulus, density, and compressive strength of a bone [16, 17, 18].*

Bone	**Young's modulus (GPa)**	**Density (g·cm $^{-3}$)**	**Compressive strength (MPa)**
Cancellous bone	0.01–0.5	0.2-2	0.2-20
Cortical bone longitudinally	11–21 (up to 55)	2.5	70-280
Cortical bone transversely	5–13	2.5	~ 50 (up to 150)

Toughening mechanisms

Bones exhibit several toughening mechanisms ranging from nanoscale to macroscale. At the nanoscale, toughening (plasticity) is achieved by molecular uncoiling and intermolecular sliding. At higher levels, plasticity is exhibited through microcracking and fibrillar sliding. When it gets to micrometer dimensions, the breaking of sacrificial bonds at the interfaces of fibril arrays leads to increased energy dissipation and crack bridging

by collagen fibrils. At the largest scale, in hundreds of micrometers, crack deflection reduces fracture energy [18, 19].

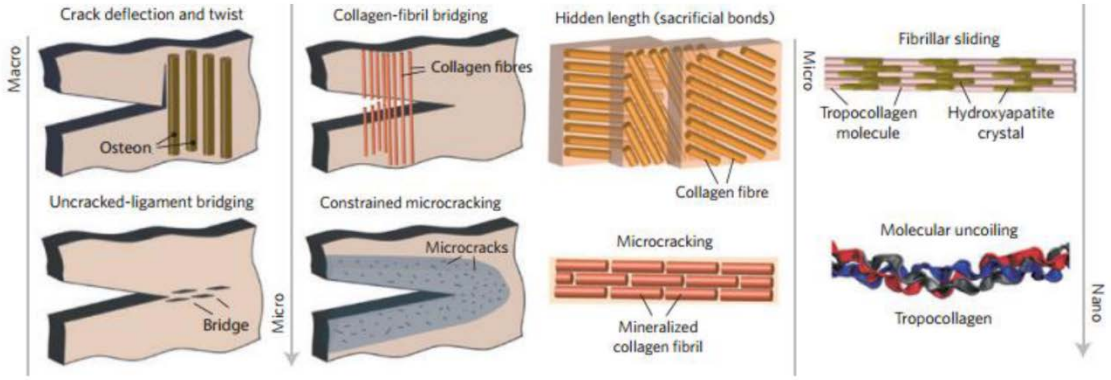

***Fig. 3**: toughening mechanisms of bone represented from nano scale to macro scale [19]*

1.2 Bone scaffold 3D printing

There are many known ways to fabricate feasible biomimetic bone substitutes. To precisely control the porous structure of scaffold, additive manufacturing techniques, also known as 3D printing, were adopted. These techniques utilize computer-aided design (CAD) which allows the production of patient-specific scaffolds directly from a computer. Furthermore, the use of medical imaging technologies like magnetic resonance imagining (MRI) or computer tomography (CT) allows for very detailed constructs. These are then built-in layer-by-layer fashion using liquid, powder, or processed solid sheets [20, 21, 22].

3D printing technologies used for biomedical applications can be separated into four groups: (1) particle fusion-based methods, (2) light-induced methods (photopolymerization), (3) inkjet printing. (4) extrusion-based methods. Using the right technique determines if biomaterial will be printable. In general, it's possible to print the same material using different approaches but the form and composition of material change from technique to technique [22].

1.2.1 Particle fusion-based 3D printing

This group includes particle binding (PB) and selective laser sintering (SLS). Both of these methods become popular in industrial prototyping mainly due to their ability to print complex geometries from all commercially used materials (metals, ceramics, polymers, composites) [23].

Selective laser sintering

SLS is a method utilizing a laser beam directed in a pattern over a cross section of a computer modeled object, to raise the temperature of used material above its melting point with the goal of fusing it together. After the material fuses, creating a single layer, another layer of powdered material is added, and the process is repeated. The method requires the use of ink consisting of fine particle powder, in the range of 10 to 100 μm, which is able to melt and bind together when heated. With the use of such a fine powder, surface functionalization may be required to ensure good particle flow dynamics. Among the disadvantages of SLS are the dimensions and price of machinery used. Nonetheless, the capability to process multiple materials in one bed proves to be very practical for certain manufacturing industries [23, 24, 25].

Particle binding

PB functions in principle the same way as SLS. But unlike in SLS, fusion is not achieved by melting the material using a laser, but instead by adding a binding solution with each layer and sintering the final 3D object in postproduction. The method finds less use in later years thanks to the sufficiently powerful laser which does not require post-production treatment [25, 26].

1.2.2 Light-assisted 3D printing

A method known as stereolithography (SLA), was coined as the original additive manufacturing technique developed by Charles Hull in the 1980s. The process involves the use of light, UV or laser, to map a specific area followed by curing a liquid resin (photopolymerizable), creating a single hardened layer. Another layer is created by lowering the platform into the solution and polymerizing a new layer on top of the previous one [27].

SLA offers a very high resolution compared to other printing methods, achieving from 25 μm to1μthe m with the use of a more advanced high-definition SLA. Unfortunately, biomedical applications are very limited due to many factors. The use of UV light, need for postprocessing, bad mechanical properties, contamination by unreacted monomers and the lack of usable biocompatible materials makes it hard to utilize in tissue engineering [22, 28, 29].

1.2.3 Inkjet Printing

The technique of inkjet printing allows for deposition of very small volumes of material. The material takes the form of droplets and is deposited onto a printing surface where it takes the form of a structure after solidification. They can be separated into two groups: (1) continuous inkjet printing (CIJ); (2) drop-on-demand inkjet printing (DOD). As the name suggests in CIJ, droplets are deposited continuously, whereas in DOD droplets are produced as required [30].

There are three stages in inkjet printing which define the usability of chosen material:

(1) drop generation; (2) interaction between droplet and substrate; (3) drop solidification. But by far the most important properties of suitable ink is its viscosity and surface tension, where viscosity should be low enough to secure the creation of reproducible droplets and surface tension determines the shape of the drop. For the applications in biomaterial engineering, polymer melts, photocurable solutions, colloidal suspensions and even ceramics were used successfully. Although, there are many problems connected with usability of inkjet printing for biomedical purposes, they found some use in tissue engineering and pharmaceutical applications. [30, 31, 32, 33].

1.2.4 Extrusion-based 3D printing

Extrusion based 3D printing belongs between the most widespread production methods thanks to its low price and wide range of usable inks. Its basic and direct production approach makes it simple for researcher to adopt and adjust for a wide range of uses [21, 34]. It can be divided into two main groups. Fused deposition modeling (FDM), and direct ink writing (DIW). Both methods work on the same principle, where viscous ink is forced through a nozzle following a computer designed path depositing material in layer-by-layer fashion. Viscosity plays an important role in stability and rigidity of layers. If it's not high enough, layers won't offer sufficient support for successive layers and if it's too high, ink won't be able to be extruded [10, 34].

Direct ink writing

Direct ink writing utilizes deposition of ceramic slurries or polymeric solutions. The process requires a driving force to extrude. Driving force can be obtained in a form of air pressure which is used for pneumatic dispensing, or mechanical forces for piston and screw-driven dispensing. Pneumatic dispensing allows for precise control of the applied force by controlling the air pressure, which in turn permits accurate adjustments for material deposition. On the other hand, deposition by mechanical force uses a plunger operated by a motor which offers more sophisticated control, like variable extrusion speeds and retraction. System of DIW offers for even more adjustments, such as nozzle size and nozzle geometry [35, 36].

There are many ways to set up a successful DIW for tissue engineering. When hurdles occur, it's usually not with the technology but with the material used in the ink. Rheology is a very important for printability, and every ink has its specific demands for its viscosity depending on the printing process. For the material to be able to be extruded through the needle, it needs to show shear thinning behavior. After the extrusion, quick shear recovery needs to occur in order for the material to retain its plotted shape [36, 37].

All the aforementioned methods have to use utilize elevated temperatures or postprocessing, both of each are not an ideal environment for incorporation of biologically active molecules and cell cultivation. But the use of ceramic slurries able to go through setting mechanisms in low temperature, offers a great alternative, which can be used in DIW. These will be greatly utilized further in this thesis [39].

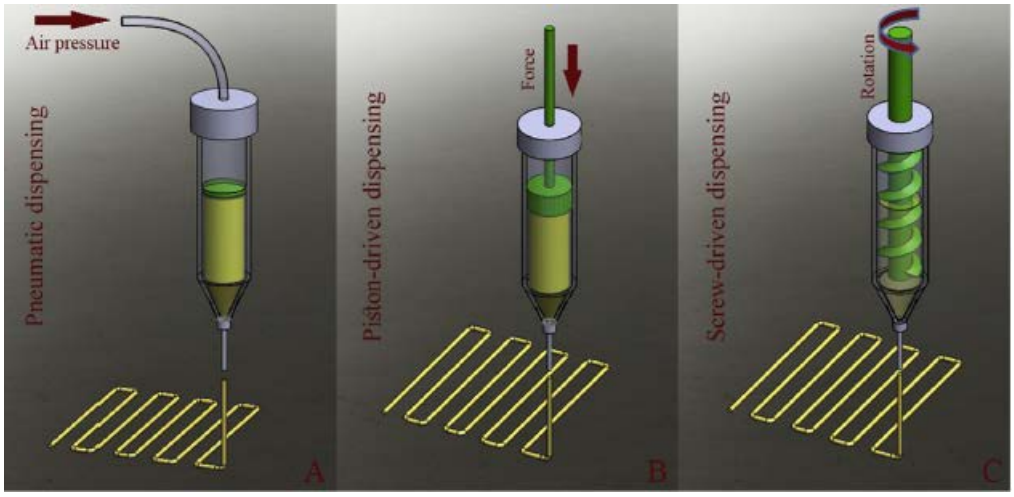

Fig. 4: *Graphic representation of DIW methods. (A) pneumatic, (B) Piston-driven, (C) screw-driven dispensing [34]*

1.3 Materials for 3D printed bone scaffolds

1.3.1 Ceramics - calcium phosphate cement/bone cement

Ceramic materials for biomaterial use, exhibit exceptional biocompatibility. Their composition highly resembles the mineral phase of natural bone. They can be divided into categories by the degree of their interaction with tissue: (1) nearly inert; (2) porous; (3) bioactive; (4) resorbable [40].

Calcium phosphates are used in a wide range of adjustable bioceramics for repair of hard tissue. Most of them prove to be osteoconductive and in some cases even osteoinductive. The ability to possess such attributes is influenced by subtle variations in chemical and physical makeup of calcium phosphate ceramics. Surface chemistry, surface charge stoichiometry, and crystallinity are among many factors influencing cell differentiation [41].

Combinations of CaO_2 and P_2O_5 with and without water yield a large variety of calcium phosphates (Ca/P). Among the most common are hydroxyapatite (HA), β- and α-tricalcium phosphates (β-TCP, α-TCP), amorphous calcium phosphates (ACP), calcium-deficient hydroxyapatite (CDHA) and their combination (BCP) [42].

Table 2. *Properties of CaP influencing osteoblastic differentiation [41].*

	Ca/P ratio	**Solubility (K_{sp})**	**Osteoinductivity**
Hydroxyapatite	1.67	Poor (10^{-58})	+
Tricalcium phosphate	1.5	Fair (10^{-25}–10^{-29})	++
ACP	1.15–1.67	High (10^{-23}–10^{-25})	+++
BCP	1.5-1.67	Depends on TCP/HAP ratio	++++

Tricalcium phosphate (TCP)

Hydroxyapatite (HA; $Ca_{10}(PO_4)_6(OH)_2$) was for many years the main focus of research in the field of calcium phosphate materials. As a nearly inert material, not well suited for bioactive purposes, the focus lately shifts to more reactive materials. Composites combining HA and β-tricalcium phosphate (β-TCP; β-$Ca_3(PO_4)_2$), standalone β-TCP, and in recent years α-TCP, octocalcium phosphate (OCP), dicalcium phosphate dihydrate (DCPD) and anhydrous dicalcium phosphate (DCP) [43].

After hydroxyapatite, TCPs are the second most dominant phase found in human bones. It grown in popularity thanks to its faster resorption profile compared to hydroxyapatite. In general, TCP combines with bone tissue without rejections and after incorporation into a desired area of bone defect, supplies the bone with Ca and P ions propagating formation of a new bone. Tricalcium phosphates ($Ca_3(PO_4)_2$) can be found in three substitutes, which include α-TCP, β-TCP and α′-TCP. α′-TCP is not a stable modification and exist only above temperatures of 1430 °C. Below this temperature it transforms into a metastable α-TCP modification. Another way to obtain α-TCP is by transformation of β-TCP, which transforms above the temperatures of 1125 C. As a metastable modification, it tends to transform back but can be retained during cooling to room temperature [44].

Even though they are substances with the same chemical structure, different modifications possess different properties like structure, density, solubility. Structure of α-TCP is polygonal while β-TCP is spherical, more trabecular, and porous. β-TCP finds the most common use out of all the modifications. It resorbs faster than α-TCP and when compared to HA its resorption is 10 to 20 times faster. Mostly it is used in a form of macro porous granules and blocks, where it shows similar compressive strength as cancellous bone, but alone proves to be brittle with low tensile strength. On the other hand, α-TCP finds more use as a fine powder, with high solubility utilized in preparations of calcium phosphate cements. After mixing with liquid phase, it forms a hard material, which is suitable both as direct filling for bone defects and connecting interface for joining another biomaterial with bone tissue [45, 46]. Moreover, α-TCP reacts with water, as shown in eq.1 forming calcium deficient apatite crystals, leading to a high

biocompatibility [47].

$$3Ca_3(PO_4)_2 + H_2O \rightarrow Ca_9(PO_4)_5(HPO_4)OH \quad (1)$$

1.3.2 Polymer - ceramics calcium phosphate cement

Incorporation of polymer, either of synthetic or natural origin in CPC formulations is attracting a lot of attention. It can be integrated as a second solid phase or a water solution. Both prove to be excellent choices for improving CPCs properties like their cohesion, injectability, setting time which are crucial for clinical use but also resorption rates and tissue response [48].

Both setting time and cohesion, are influenced by the change in viscosity of the CPC paste, which is in general higher after the addition of polymer. For setting time, higher viscosity inhibits ion diffusion in the matrix, whereas in cohesion (washout resistance) fluids are prevented from penetration by higher viscosity. When it comes to good injectability, its mostly desired by medical professionals as it allows for adequate filling of complex defects in minimized surgical procedures. It can be increased by adjusting L/P ratio, however, this can have negative effects on mechanical properties. When it comes to mechanical properties, CPCs have been largely limited for nonload-bearing applications due to their low performance. Incorporation of polymer can improve performance by increasing ductility, toughness, and overall strength [48,49,50].

There is a big array of both natural and synthetic polymers used in CPCs. Among natural polymers used are collagen; alginate; hyaluronate; chitosan; cellulose; and many more less studied natural polymers. Between synthetic polymers commonly used are polyesters and polyethers; polyacrylic acid and fibrin glue. Natural polymers are mainly used in liquid phase which can be well dissolved in water. On the other hand, synthetic polymers are preferably used in solid phase as they are not so easily dissolved in water [50].

1.3.2.1 Chitosan

Chitosan is a linear, semicrystalline polysaccharide composed of randomly distributed N-acetyl-D-glucosamine and D-glucosamine units, derived from chitin. It can be found exoskeletons of crustaceans or cell walls of fungi. It is not soluble in water but can be dissolved under acidic conditions. Among many properties which make it hugely popular for biomedical applications, belongs biodegradability, biocompatibility but also antibacterial, antifungal activity, mucoadhesivity etc. Most of these can be attributed to its cationic nature. [51] Furthermore, there were reported significantly reduced setting times, and positive effects on flexural and compressive strength where the highest values were obtained with 15-20 wt.% [52].

1.3.2.2. Copolymer PLGA-PEG-PLGA

Even thou calcium phosphate bone cements (CPC) offer significant potential in the field

of hard tissue repair; they still miss some critical attributes. Especially their poor injectability at low force levels, bad washout resistance to body fluids after mixing and high solid contents without separation. These can be worked around with the use of augmentation of CPCs by polymeric additives. There have been reported use of multiple polymers with the goal of improving properties of CPCs, like collagen hydrogels, chitosan, gelatin, hyaluronic acid, water-soluble poly(ethylene glycol) and much more. More interestingly, an innovative CPC augmented by thermo-responsive copolymer (poloxamer) was used, thermogelling at body temperature. That leads to increase of viscosity of the CPC right after the injection into the body, improving washout resistance. Unfortunately, the use of poloxamer was not ideal but it showed a promising way for using copolymers for supplementation [53].

One such copolymer is poly(lactic acid), poly(glycolic acid) and poly(ethylene glycol) (PLGA-PEG-PLGA), which behaves in very similar way as poloxamer. PLGA-PEG-PLGA is a triblock copolymer formed by either A-blocks or B-blocks, which arrange themselves into an ABA or BAB type. They prove to be soluble in water, but form depots at biomimetic conditions after injection. Solubility at room temperatures leads to good injectability due to its thixotropic behavior. After application in the body, PLGA-PEG-PLGA is fully biodegradable, where it safely degrades into CO2 and water. Furthermore, successful release of drugs and proteins in the span of 1 to 6 weeks was reported, but because of poor functionalization is very limited [54]. Specifically, functionalization of copolymers is drawing attention in later years, as it offers its sol-gel and gel-sol phase transitions to subsequent composites. These present prospects for emergence of novel CPCs closer to ideal [53, 55].

1.4 Architectural parameters of scaffolds

Studies in recent years emphasized the importance of proper scaffold design for successful cell attachment, migration, proliferation, and differentiation. Initially composition and surface chemistry play the primary role for cells to attach but in later stages morphology becomes the main factor in controlling their ability to migrate. Moreover, the right architecture secures nourishment of cells, flow of oxygen and removal of waste products, which increases the survivability of cells and as a result leads to a formation of new tissue. Hence, the design must incorporate porosity which is interconnected with pores large enough for cells to allocate correctly. On the other hand, scaffold must retain its mechanical properties which are known to be significantly affected by porosity. Based on this, structural properties like pore size, pore distribution, pore morphology and interconnectivity play the most important role in scaffold design [56].

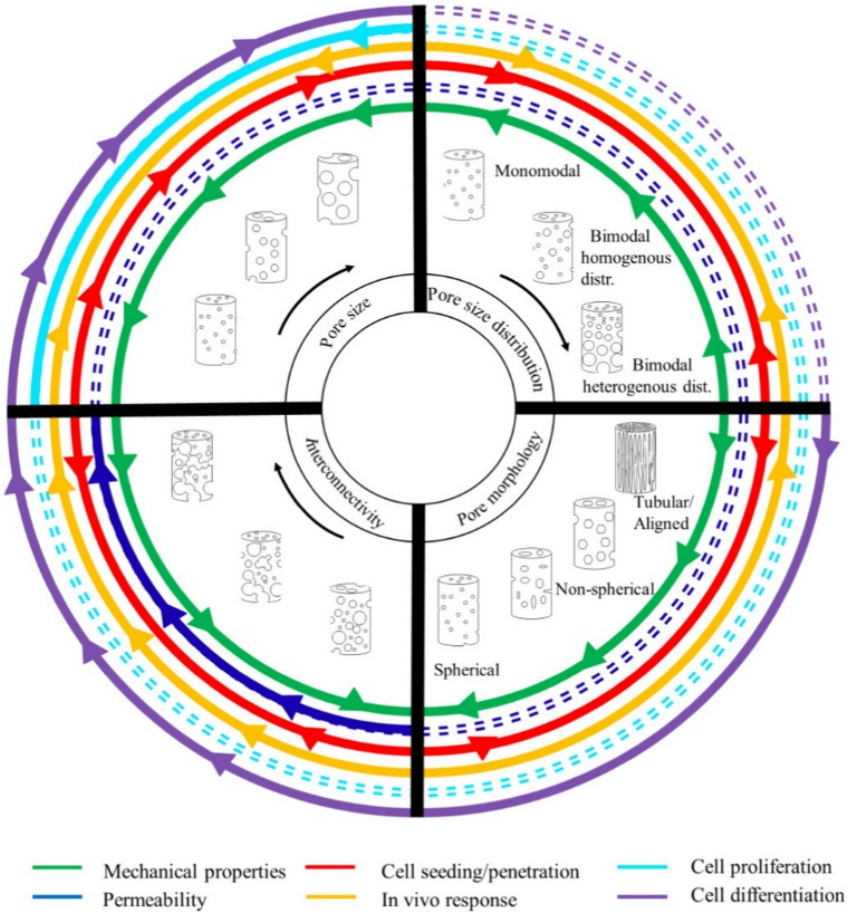

Fig. 5: *Effects of structural properties on physico-chemical and biological behaviors [56]*

1.4.1 Pore Size

Porosity is defined as quantification of void spaces within a material. When it comes to porosity of dense materials, IUPAC defines three different types: micropores (<2 nm), mesopores (2–50 nm) and macropores (>50 nm). Classification changes slightly when it comes to use in tissue engineering, where biomaterial engineers divide porosity into macropores (>50 μm) and micropores (<50 μm). This classification will be used further in this thesis. Porosity can be measured by methods which utilize flow, such as mercury intrusion porosimetry or by imaging methods like scanning electron microscopy (SEM), micro computed tomography (μCT) and atomic force microscopy (AFM). All of the aforementioned methods use slightly different approach to determine the pore size and pore distribution obtaining slightly different resolutions [56].

1.4.2 Macroporosity

Macroporosity plays a key role in tissue regeneration. Its main role is to let cells penetrate the scaffold and allow the integration with host tissue to occur, which in turn can lead to occurrence of key processes like blood vessel ingrowth to take place [56]. Optimum pore

size was studied extensively for a few decades at this point, but there still isn't uniform conclusion as to which is ideal. There was reported use of mean pore sizes ranging from 20 μm to 1500 μm [57, 58, 59]. Early reports established that for any significant bone growth to occur, the optimal pore size is somewhere in the range of 100-135 μm [59]. Since then, more recent studies suggest that for bone formation and vascularization to occur within the scaffold, pores need to exceed 300 μm. Pores that meet these requirements facilitate capillary formation, which in turn leads to direct osteogenesis while pores smaller than 300 μm can encourage osteochondral ossification. This has been demonstrated by greater penetration of bone and better integration in scaffolds with larger pore interconnections in small well-connected pores, rather than in large, isolated pores. However, the need to limit the maximum pore size, which has a significant negative effect on the mechanical properties of the scaffold, should not be neglected either. [61, 62] Nevertheless, even if the ideal pore size is established and used, it is still not clear if the use of homogenous or heterogenous distribution is more efficient [63].

1.4.3 Microporosity

Microporosity is defined under the surface topography as small pores with diameter below 10 μm [56]. Within the ceramic scaffold it can occur either as closed or open microporosity, where closed micropores does not engage with cell microenvironment but affect the mechanical properties. While it was recognized that the rate of integration and volume of regenerated bone is mainly depended on macroporosity, recent studies started to recognize the importance of microporosity in ceramic scaffolds. Mainly their tremendous effect on cell proliferation and differentiation. Furthermore, its ability to increase osteoconductive capacity of material by improving protein adhesion can't be overlooked [64]. Habibovic et.al [65] reported that the presence of microporosity was necessary for successful osteoinduction. Another study reported formation of denser bone in early stages with increased levels of microporosity [66]. Regarding the effects of microporosity on bone regeneration, the results vary depending on their observation *in vivo* or *in vitro* [64].

Numerous mechanisms have been proposed as to how microporosity effects cell and tissue behavior. It was proposed that microporosity provides anchoring sites for cells extensions (filopedia), permitting them to spread through material. However, Annaz et.al [67] concluded in the same report that this mechanism is not necessary and only has effect in early stages of implementation. Another mechanism proposes that microporosity and, in extension, surface roughness enhances selective adsorption of serum proteins which in turn positively influence adhesion of cells and general cell behavior [67, 68]. Moreover, surface microporosity increases the specific surface area of scaffolds, leading to faster dissolution and reprecipitation of CPCs ions (Ca, P) resulting in formation of biological apatite [65].

1.4.4 Pore morphology

Pore morphology belongs to another important factors influencing biological response and cell behavior, especially at macropore scales. Rumpler et.al [69] concluded that cells tend to respond to radii of curvatures fare larger than themselves. In his report, osteoblast like cells cultured on hydroxyapatite with different cross sections, showed initial formation of tissue at corners and subsequent growth in circular fashion. Thus, it can be proposed that tissue growth is curvature-driven, resulting in round openings no matter the initial unit cell shape [70].

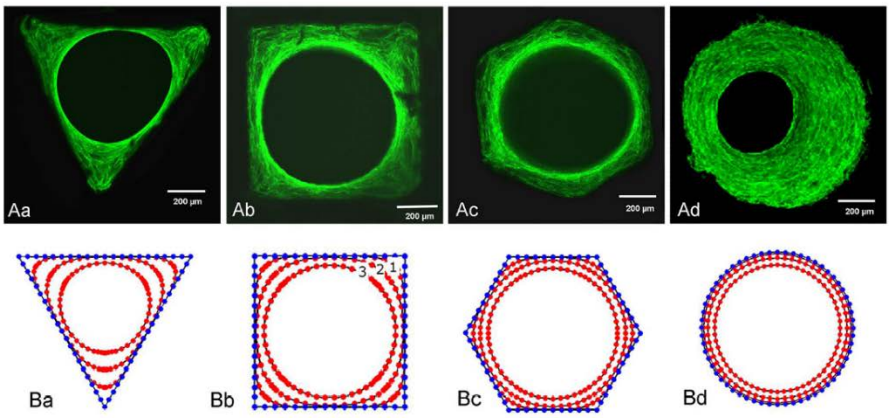

***Fig. 6**: Observed tissue growth in channels with controlled geometry Aa) triangular, Ab) square Ac) hexagonal, Ad) circular [69]*

1.4.5 Geometrical design of scaffold

Aforementioned factors in bone tissue engineering highlight the importance of intrinsic structure in scaffold architecture design, which does not only influence cell behavior but mechanical properties [7].

Advances in additive manufacturing have allowed extensive control over the total porosity, size and morphology of pores and their distribution. Over the years many unit cells were proposed and tested with the goal to establish general rule for unit selection and scaffold design, but universal characterization method for porous structures is still missing [71, 72, 73]. Fig. 7 offers examples of frequently used scaffold architectures based on different types of unit cells.

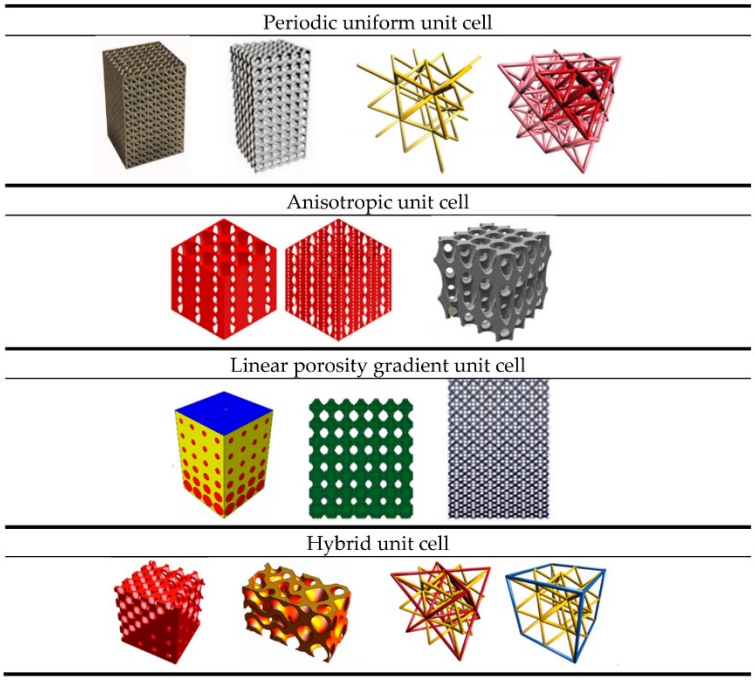

***Fig. 7**: Scaffold designs divided by unit cells used [7]*

1.4.6 Auxetic structures

Auxetic materials are gaining attention in later years mainly due to their peculiar behavior and probable enhanced properties compared to their conventional counterparts. These include energy-absorbtion, buckling resistance, shear resistance, hardness of material (indentation resistance) etc [74].

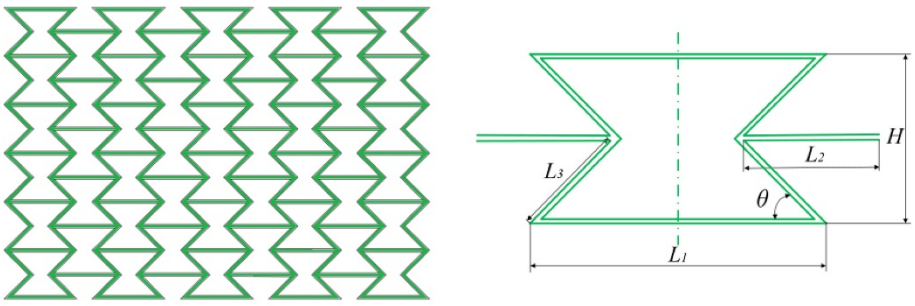

***Fig. 8**: Geometry structure of auxetic reentrant honeycomb [80]*

Unlike the vast majority of materials which undergo transverse contraction when stretched in the longitudinal direction, auxetic material expands in lateral direction when stretched or contracts laterally under uniaxial compression. This will culminate in negative Poisson's ratio, which is the key to behavior of auxetic materials. Subsequent advancements in fabrication methods found a wide range of use in all major classes

covering metals, polymers, textile, composites, ceramics but most importantly biomaterials [75, 79]. With the emergence of additive manufacturing, production of auxetic materials with tailored structures passed into commercial sphere of use. Studies reported a successful use of several methods like selective laser sintering, electron beam melting and direct laser writing [76,77,78, 79]. Use of AM methods like DIW has many hurdles to overcome when it comes to production of auxetic structures. Main concerns arise around the accuracy required for manufacturing of auxetic structures which are composed of complex shapes. These can be hard to acquire with the use of DIW especially when it comes to extrusion of paste, and precise optimalization of the process will be required.

Implementation of auxetic structures into biomaterial scaffolds is a novel idea yet to be researched more closely. Vijayavenkataraman et. al [81] proposed a new design of bone plate incorporating auxetic structure to decrease the stiffness of the region to enable intra-operative bending. Re-entrant honeycomb and missing rib structure were utilized in this work. Vijayavenkataraman et. al concluded that the Re-entrant honeycomb structure served as an effective bone design compared to conventionally used designs. In another study, Jin et.al [82] proposed a use of new method for design and fabrication of tunable auxetic scaffolds using melt electro writing (MEW). Report concluded a successful use of MEW technique more suitable for some biological applications, especially where scaffolds require special mechanical cues.

1.4.7 Gyroid structures

Complex mesh designs are gaining a lot of interest in the field of tissue engineering. One such structure is a gyroid. It belongs into a family of triply periodic minimal surfaces (TPMS). TPMS are surfaces with zero average curvature and are characterized by minimizing local area, which means that each sufficiently small patch removed from TPMS has the smallest area of all patches created below the same limits. These can create surfaces dividing space into continuous phases, with high surface to volume ratio providing large surface area for cell adhesion at a certain volume fraction. Structure is generated according to the eq. 2, where L decides the length of the unit cell cube and the parameter "t" determines the size of the cross-sectional diameter of the struts, and thus affects the most important characteristics of the gyroid structure and that is the relative density, often mistaken for the volume fraction of the solid phase [83, 88]:

$$sin\frac{2\pi x}{L}cos\frac{2\pi y}{L} + sin\frac{2\pi y}{L}cos\frac{2\pi z}{L} + cos\frac{2\pi x}{L}sin\frac{2\pi z}{L} - t = 0 \quad (2)$$

Parameter “t” defines gyroid as a single-gyroid structure. Its value can move in interval $\in$<-1.5; 0; 1.5 >. Change of parameter “t” influences the curvature of the structure in one way or another depending on the value. $0< |t| \leq 1{,}413$: In this range, the structure is interconnected with increasing or decreasing volume fraction of the half-spaces forming

the gyroid structure. Value of 1,413 its limiting, where after the parameter “t” exceeds 1,413, the surface is no longer interconnected [89].
When two single-gyroid structures with the opposite orientation of the curvature of its surfaces get interconnected, double-gyroid is formed. Similarly, as in single-gyroid, value for parameter “t” lays in the range of $0< |t| \leq 1{,}413$. Its structure is generated according to eq. 3 [89]:

$$\big(cos(x) \cdot sin(y) + cos(y) \cdot sin(z) + cos(z) \cdot sin(x)\big)^2 = t^2 \qquad (3)$$

Porous structures, such as gyroid, offer significant advantages. They are lightweight and the use of material is reduced due to their adjustable porosity. These allow for adjustments of their mechanical properties. Ma et. al [88] in this study highlighted mechanical properties of gyroid structure used to fabricate bone-mimicking scaffold. They fabricated scaffolds using metallic alloys with three different porosities and thicknesses of walls, which all proved to have elastic moduli in the range of trabecular bones. There were differences in values of stress strain curves, but in general results were very similar. Noticeable difference was observed in elastic modulus, where the highest value obtained the samples with lowest porosity. This suggest that porosity has much bigger influence at mechanical properties than the width of the walls. In terms of mass transport properties, they concluded that gyroid structure is suitable for bone scaffold design. Use of alloy material differs from the use of CPCs in this thesis but the conclusions that gyroid is a structure usable and ultimately tunable for use in bone tissue engineering proves to be beneficial for our purposes.

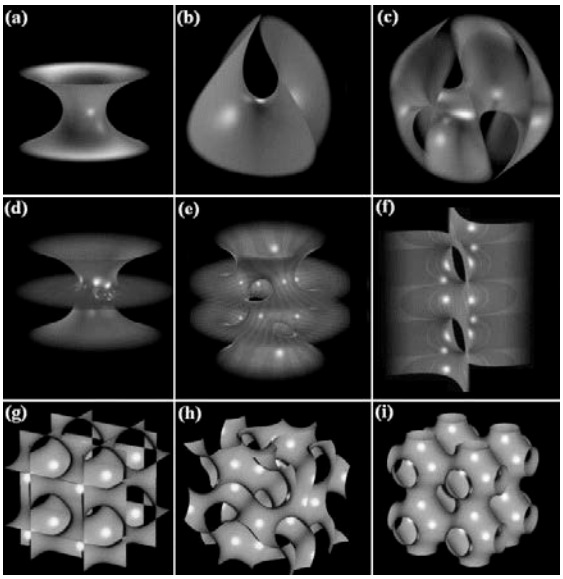

Fig. 9: *Mosaic of known minimal surfaces unit cells [90]*

When it comes to manufacturability, gyroid structures proves to be self-supported which

suits very well with AM methods, especially with DIW of ceramic paste where printed structures do not need additional support structures. Gyroid morphology consist of units made of quadruple junction points, where branches of the mesh have curved shape and link other nodes throughout the structure. Mesh created in this way offers interesting features for biomaterial scaffolds. Mainly, its mechanical energy absorption and robust structure as well as good nutrient and waste flow thanks to its high porosity and minimal surface area [84]. Olivares et al [86] indicated in his report that gyroid structure has better interconnection and proves to be more accessible to fluids than hexagonal structure, which can yield good ability to seed cells and transport nutrients. In another report Jung et al. [87] indicated that gyroid structures has isotropic elasticity. Interesting property of gyroid structure is that its inherently chiral, where its mirror image cannot be transformed to coincide with itself by translation and rotation [85].

2. MAIN GOALS OF THE WORK

In accordance with the literature search, the following objectives have been established for this thesis. The main goal was to study the effects of morphology on novel porous polymer - ceramic material prepared by the method of additive manufacturing. More precisely, extrusion-based method of direct ink writing was utilized, to print scaffolds made of composite paste mixture, comprised of biodegradable copolymer, biopolymer, and calcium phosphate cement. To study the effects of morphology, different unit cells like honeycomb and gyroid structures will be utilized. As this thesis employs the use of novel fabrication processes and implementation of modestly explored morphology in 3D printed bone scaffolds, proper optimalization will be thoroughly described.

To solve these goals, research will focus on:

- Development of computer assisted designs of infill structures for use in CPCs scaffolds.
- Optimalization of fabrication method, with the goal to produce desired scaffolds successfully and reproducibly.
- Study of relationships between morphology and mechanical properties.
- Determination of best suitable internal structure for their mechanical properties in 3D printed CPCs scaffolds

3. EXPERIMENTAL PART

3.1 Chemicals

- PLGA-PEG-PLGA triblock copolymer.Prepared by ring opening polymerization under nitrogen atmosphere. D, L-LA/GA molar ratio of 3.0 and a PLGA/PEG weight ratio of 2.5. Molecular weight (M_n = 5600 Da). Synthetized at CEITEC BUT by Ing. Klára Lysáková.
- Polyethylene glycol (PEG), Mw 1500 $g.mol^{-1}$ was purchased from Sigma-Aldrich (Germany)
- D,L-Lactide (LA, ≥ 99.5%) was purchased from Polysciences (PA, USA)
- Glycolide (GA, ≥ 99.9%) was purchased from Polysciences, (PA, USA)
- Tin octanoate (SnII 2-ethylhexanoate, ≥ 92.5%) was purchased from Sigma-Aldrich (MO, USA)
- Low molecular weight (100 000 Da) Chitosan ChitoBiomer 1219 ProfiBone. Manufactured by Genis hf., Iceland
- Polyethylene glycol 400 Merck KGaA (Darmstadt, Germeny)
- Alpha-Tricalcium Phosphate manufactured by INNOTERE GmbH, Germany. Partical size <63µm.
- Ultrapure water (Ultrapure watere of Type I according to ISO 3696) was prepared on Millipore purification system (MilliQ Academic, Millipore, France)

3.2 Equipment

- ZMorph VX FAB 3D printer (Poland)
- Planetary centrifugal mixer ThinkyMixer ARE-250 (Japan)
- Microscope Leica TL3000 Ergo from LeicaMicrosystems (Switzerland) LTD
- Flexacam C3 microscope camera (Germany)
- Cooled incubator VWR IL 68R (VWR International, USA)
- Incubator (CO2Cell 190 Standard, MMM-group, Germany)
- Analytical scale AB204-S (Mettler-Toledo, s.r.o, Czech Republic)

3.3 Sample preparation

3.3.1 Synthesis and Purification of PLGA-PEG-PLGA Copolymer

Thermosensitive poly(D,L-lactic acid-co-glycolic acid)-b-poly(ethylene glycol)-b-poly(D,L-lactic acid-co-glycolic acid) triblock copolymer (PLGA-PEG-PLGA) with LA/GA molar ratioequal to 3.0 and PLGA/PEG weight ratio equal to 2.5 was synthesized

under nitrogen atmosphere via ring opening polymerization method in a bulk at 130 °C according to Michlovská et al. [91]

3.3.2 General preparation of calcium phosphate cement paste

Phosphate bone cement paste was composed of liquid phase and solid phase. Copolymer PLGA−PEG−PLGA was dissolved in ultrapure water in a ratio to achieve solution of 20 wt.%. Dissolving copolymer was mixed extensively in 12 °C for 3 to 5 days to achieve perfect dissolution. The required amount of dissolved copolymer was taken and 3 wt% of low molecular weight chitosan powder based on the weight of the copolymer mixture was added and extensively mixed. Further was added 4 wt.% of plasticizer in the form of liquid PEG 400 based on the weight of the previous mixture and homogenized. Final weight of the mixture was taken to calculate the addition of (α-TCP) powder in L/P (liquid/powder) ration of 0.65 were PEG and copolymer represented the liquid and chitosan and α-TCP represented powder. Mixture was extensively mixed one last time after the addition of (α-TCP), achieving calcium phosphate cement paste and used in quick succession.

3.3.3 3D printing

3D printing parameters on the Zmorph printer were set as follows: filament height 0.35 mm; extrusion coefficient 0.14; printing speed 7.5 mm. Desired G-code of block samples with dimensions of 6x6x12 mm is then imported into the operative software, Voxalizer, and 3D printer is set into its home position. This position can be considered as a starting position where its axis Z is then set to zero using internal controls allowing us free movement of the printer head in all directions. Separate sheet of glass is then covered with parafilm and placed into the printer serving as printing surface. Sheet is secured in its positions by spraying a small amount of water under it, utilizing surface tension, successfully preventing any movement during the 3D printing process. Next, sealable container is filled with ultrapure water and placed in a heated incubator to create a humid environment later used in sample curing. With all the necessary pre-requirements ready, CPC paste is prepared as described above. Prepared paste is filled into a syringe using spatula, injection tip is attached, and everything is placed into its designated holder. With injection system ready, final calibration takes place, where printing head is brought over the glass sheet and is lowered close to the surface. Piece of paper is placed under the injection tip, printing head is carefully lowered as not to bend the tip, to the first point where its not possible to remove the piece of paper. Printing head is then brought few steps higher, step being 0.1 mm, as to set the height of the first layer, ranging from 0.1 mm to 0.4 mm depending on the structure about to be printed, and axis Z is once again set to zero. At this point, 3D printing process can be started using computer. The head of the printer starts by drawing circles, in order to stabilize the flow of CPC paste through the syringe, where we manually extrude the paste using a driving screw. After confirming

stable flow of CPC paste, drive screw is secured in its position by securing hat and 3D printer proceeds with the printing. Process ends after the printer either finishes the printing of imported G-code or runs out of material at which point the device is disassembled, cleaned, and prepared for next use. The finished samples are taken from the printing area together with parafilm and are placed into a sealed container which was readied in a heated incubator. Samples are cured in humid environment for three days and then transferred into a freezer where they remain until testing.

3.4 Methods

3.4.1 Determination of mechanical properties

Methodology is based on the international standard ČSN ISO 13314 intended for mechanical, ductility, and compression testing of porous and cellular metals. The test in principle consists of pressing the sample between two metal plates in laboratory temperature conditions performing quasi-static strain rates in the range of 10^{-3} to 10^{-2} s^{-1}. Procedure consists of following steps:

- measurement of the initial dimensions of the tested samples
- estimation of stable stress levels σ_{pl}
- determination of values for release of hysteresis loop - F_{20} and F_{70}
- determination of the maximum loading force F_{max}
- insertion of the sample

After initial tests, set σ_{pl} and strain rates are evaluated and verified. Following the procedure provides data which can be plotted into appropriate diagrams (stress/strain; pressure/elongation diagram). Evaluation of these diagrams provides the following mechanical parameters:

- elastic gradient E
- compressive strength R_{md}
- absorbed energy W

MTS Mini Bionix 858.02 servohydraulic test system with force sensor PM 00/22 (range 1 000 N) was used for mechanical testing, operated by FlexTest GT software.

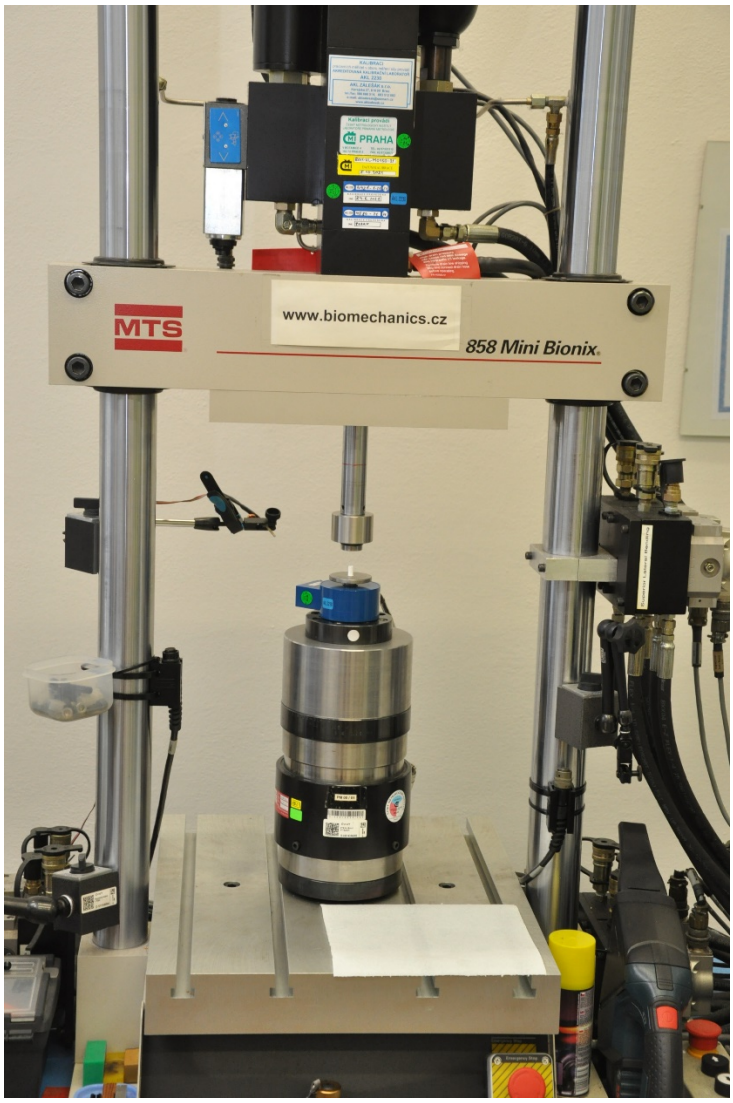

Fig. 10: *MTS Mini Bionix 858.02 servohydraulic test system*

3.4.1.1 Test sequence

Samples were removed from freezer at least hour before testing to be brought to room temperature. After the samples thawed, their dimensions of cross section a_i x b_i and height h_i were measured 3x and averaged. From their average values cross section S_0 was calculated. Samples were centered in between steel plates of MTS Mini Bionix test system and stable level of stress σ_{pl} was estimated according to previous experience. Level of stress was always adjusted according to average values achieved in the test group. During the pressure test, the pressure loading and unloading maintained a constant speed of 3.6 $mm.min^{-1}$ to achieve deformation rate in range of 10^{-3} to 10^{-2} s^{-1}. Data was recorded with refresh rate of 30 Hz. Samples are first loaded to a point before the failure of material and slowly unloaded to create a relaxation phase from which we are able to determine elastic gradient. After that, samples were loaded to a point of 50% destruction, which allows us to determine strength and absorbed energy of our structures.

3.4.2 X-ray powder diffraction (XRD)

After the samples have undergone mechanical testing, their remains were repurposed for XRD. Firstly, samples were crushed in mortar with pestle until fine homogenized powder was achieved. Appropriate amount of powder was then placed into a glass sample holder. Aligned glass sample holder was fixed inside RIGAKU MiniFlex 600 X-ray diffractometer. Measurement was conducted under angel of 2θ from 5°to 50° with speed of 5°/min at a maximum power of 40 kV and 15 mA. Measurements were conducted to establish and observe the phase compositions of CPC and conversion rates of α-TCP to CDHA.

3.4.3 Optical microscopy

Optical microscopy was utilized to observe and capture figures of infill structures. The Leica TL3000 Ergo microscope system with a Flexacam C3 microscope camera was used for this purpose. Firstly, microscope and camera were started together with computer. Magnification was set on the smalles value using dials on the microscope, and consequently in controlling software on computer. Sample was placed on microscopic slide under the microscope lens. LED lights were turned on and adjusted to ideally illuminate the observed sample, after which the image was focused and using the controlling software picture was captured.

3.4.4 Statistical analysis

Measured values were subjected to statistical analysis. We firstly subjected the values obtained to the Shapiro-Wilkinson normality test, with significance level of 0.05, which determined normal distribution of measured values. Next, it was determined that for our purposes, non-parametric Kruskal-Wallis test will be best suitable to determine statistical significance of measured values. Test was run with significance level of 95% where P-value observed at levels lower than 0.05. Values that were determined to be statistically significant were paired together in box plotted charts and marked by *.

4. RESULTS AND DISCUSSION

4.1 3D printing optimization

As was described in the first part of this thesis, 3D printing was chosen as processing method for creating our CPC constructs and as such has key role during the process, which demanded thorough and precise optimalization. The 3D printer itself has been heavily customized to suite purposes of this research, as shown in figure 11. Bulk of the optimalization (printing process parameters/ink composition) was conducted by a different researcher working on the same project, and therefore will not be discussed in detail only the chosen parameters will be mentioned.

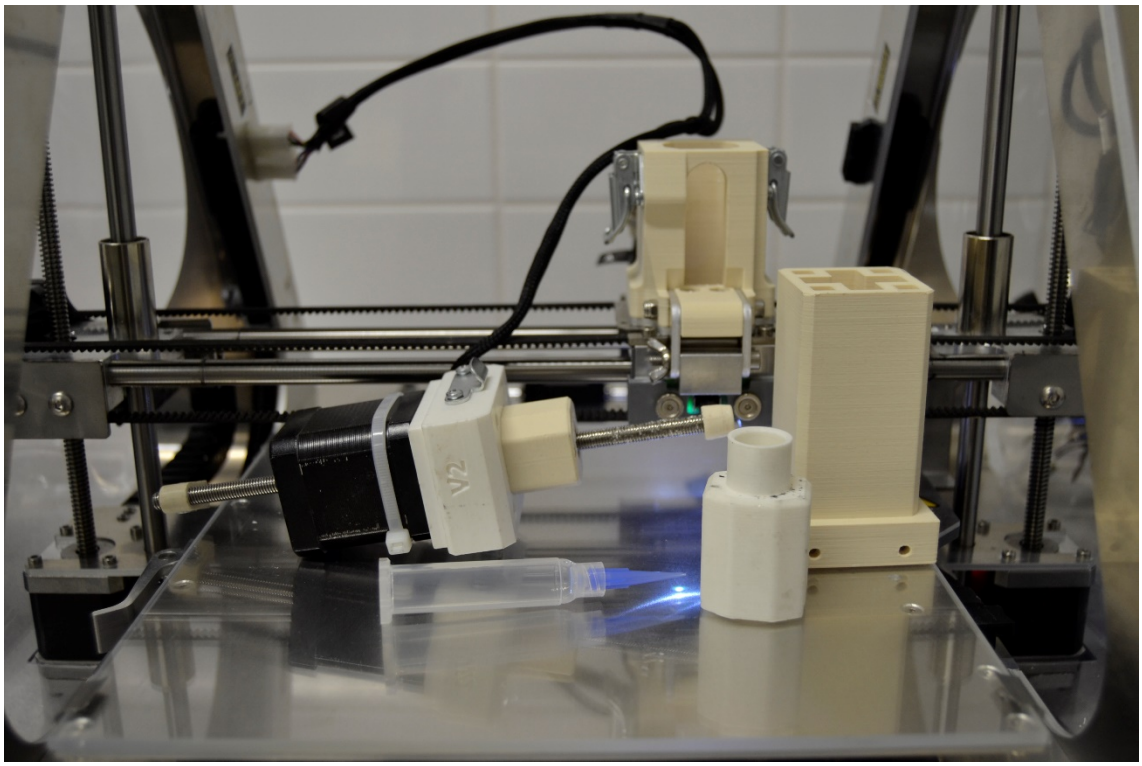

Fig. 11: *Zmorph VX FAB 3D printer - customized configuration comprised of 3D printed parts*

Chosen composition of CPC paste described in “Sample preparation section” was determined to be reliably printable and thus was not changed further for the purposes of this thesis.

Among the printing process parameters, which proved to be key for obtaining reproducible results with good resolution were extrusion nozzle, printing speed, extrusion coefficient, filament height. There were two possible injection nozzle tips tested for use, namely with diameter 250 μm and 410 μm. Both proved to be usable, but 410 μm was utilized in the process of this thesis. Printing speed played important role when it came to

resolution and consistency of each individual filament and consequently layers of our 3D printed objects. The importance became even more evident when more complicated unit structures were introduced. The maximum limit value for printing speed was set at 10 mm/s, where extruded filaments did not rupture and maintained consistent diameter and resolution. Problems arose with more complicated unit structures, like gyroid, where laid filaments exceeded borders of printed units compromising not only resolution but mechanical properties. On the other hand, minimum limit value was set for 5 mm/s where 3D printer extruded bigger amounts of CPC paste which was shown at less consistent filament diameters mainly in the corners of our units. Furthermore, lower speed naturally affected length of printing time which led to individual units being exposed to unsuitable environment for prolonged time and for the unextruded paste to solidify inside the injector. Optimal printing speed was found to be 7.5 mm/s where all the above-mentioned problems were minimized or eliminated. Extrusion coefficient changes the relative amount of flow. Its good optimalization is important to achieve a nice surface and the right width of individual walls. For our purposes, the extrusion coefficient value of 0.14 was set as it provided good reproducible results.

4.2 Shape of 3D printed samples

During the process of researching theoretical background arose a question of what shape and dimensions our 3D printed samples should have. At first, after evaluation of available sources it was decided that our samples will be printed in the shape of a blocks with dimensions of 10x10x6 mm. Such samples were in theory ideal for observing the influence of internal structure, when a large number of internal units could be implemented into the body and, as a result, to observe their influence on the mechanical properties. These samples were able to produce precise results with very high resolution as shown in Fig. 12. However, after further consultation this configuration was reconsidered mainly due to concerns of poor stress distribution which would concentrate in the corners of the body and negatively affect the real results of mechanical properties.

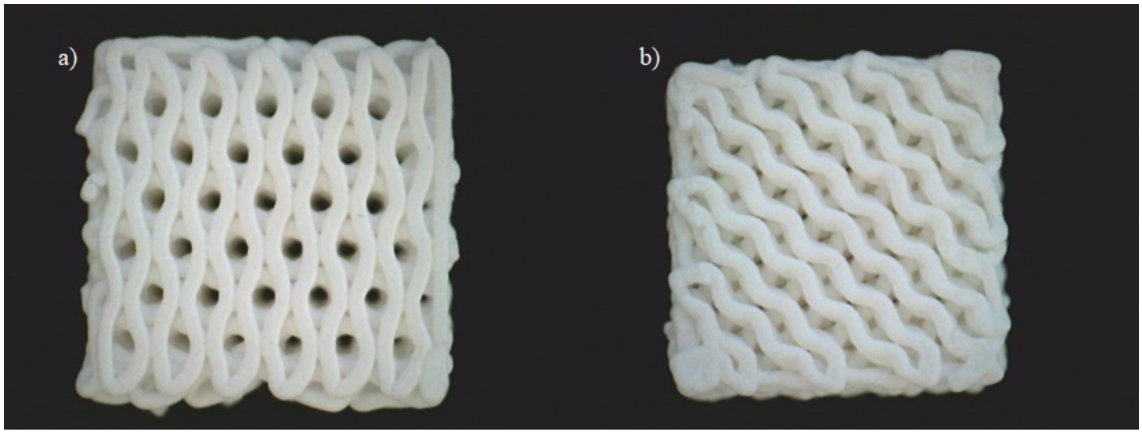

Fig. 12: *3D printed blocks 10x10x6 mm showcasing infill structure a) honeycomb; b) gyroid*

In light of these concerns new dimensions were considered, this time following the international standard ISO 13314. The standard is intended for mechanical, ductility, and compression testing of porous and cellular metals. Although not intended for ceramics, the novel character of our CPC does not have specific standards that should be applied, so the use of ISO 13314 offers the most suitable testing conditions. In accordance with ISO 13314, there were two possible choices for geometry: cylindrical cross section or rectangular cross section with the ratio of length to diameter between 1 and 2. Both choices seemed viable for our purposes and thus required further testing to discern the best suited. Consequently, both cylindrical and rectangular samples with dimensions of 6x6x12 mm were printed in two iterations of infill: gyroid, and rectilinear. 20 samples in total, 5 for each iteration. Such samples were subjected to mechanical testing where their strength and elasticity modulus were established. Ultimately, in order to distinguish which iteration will be more suitable for our purposes, the values of strength and modulus of elasticity are only indicative and can be neglected, as these are not the properties of the material but of the tested unit. Reliability and practicality of results were chosen as a decisive factor in the selection of suitable samples. To establish reliability, deformation curves of each iteration were plotted as shown in Fig. 13a representing rectilinear cylinder and Fig. 13b representing gyroid cylinder, and Fig. 14a representing rectilinear block and Fig 14b representing gyroid block. Consequently, their similarity was taken into account as well as their standard deviations. Regarding this procedure, samples with rectangular cross section were selected as more suitable for our purposes. Their deformation curves showed in Fig. 14. proved to be more regular, and their standard deviations were considerably lower. Although, it must be acknowledged that there were not enough samples tested which probably contributed to the high standard deviations for each iteration. When it came to practicality, rectangular samples were once again considered more suitable, as they were easier for handling and manipulation, which in turn led to less damage to the external structure and microfractures, thus giving better results.

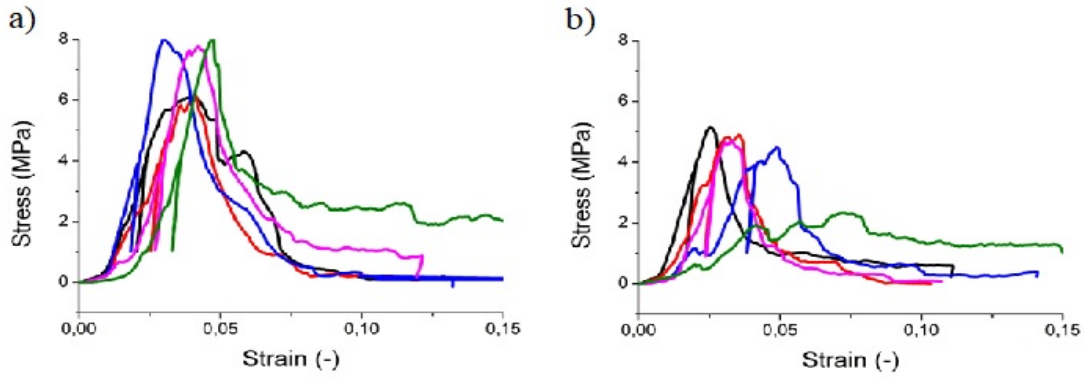

***Fig. 13**: Deformation curves showcasing course of mechanical test of a) Rectilinear cylinder; b) Gyroid cylinder*

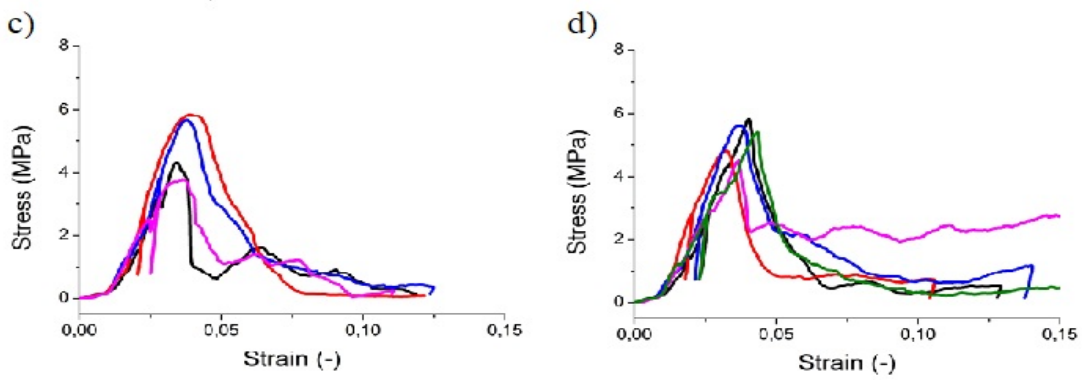

***Fig. 14:** Deformation curves showcasing course of mechanical test of c) Rectilinear block; d) Gyroid block*

4.3 Creation of customized infill design

The basis of this thesis is built around different internal structures and their influence on mechanical properties. Such structures, or infills, must be implemented using software tools usually specific to the 3D printer in use. Even though, such tools offer wide range of customization, implementing changes automatically generating desired G-codes, they proved to be lacking some key features regarding our work. Namely their catalog of prerendered infill patterns.

Fundamental idea according to which different infill patterns were approached was to maintain the same porosity of 50% while changing other parameters. Such internal structures were not possible using available software tools, thus had to be created manually.

In the beginning, functioning G-code of rectangular sample with honeycomb infill was generated as a template, from which we started to apply changes. First problem which we repeatedly encountered was the rate of extrusion. Its value set by the original templated

was not changed. Nevertheless, every iteration of our design proved that extrusion rate was not stable and let to deposition of disproportionate amount of material. Example being demonstrated in Fig. 15. Problem appeared to be tied mainly to more complex structures, like honeycomb, whereas simple structures, like rectilinear, did not experience this kind of a problem.

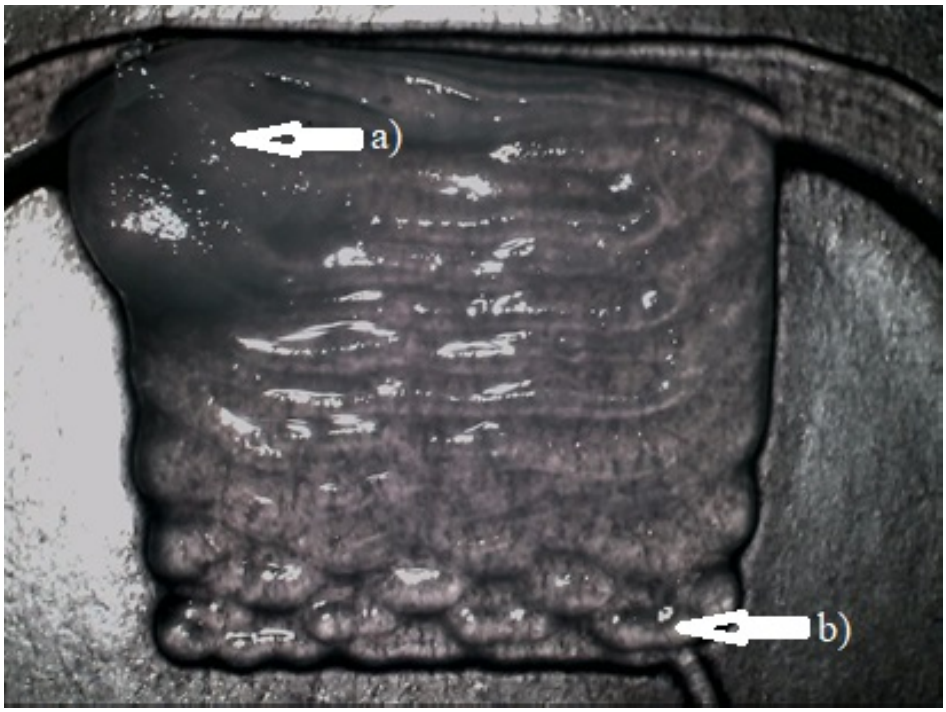

Fig. 15: *One layer of designed honeycomb structure showcasing the problem of over extrusion: a) big amount of over-extrude material; b) faint signs of honeycomb structure before over-extrusion*

This highlighted the need to better understand the internal functioning between 3D printer and adjected software. For this purpose, we introduced constant which directly influenced the speed and consequently the amount of paste extruded. Conducted experiments with rectilinear layers showed promise where we could observe decrease in the amount of extruded paste, but when it came to implementation in honeycomb layer the problem persisted. After further examination, it was determined that the persisting problem was not connected with coded extrusion speeds but rather with the printer itself. The theory was tested, where we suspected that the printer was taking into account the traveled path of its printer head, and subsequently trying to subside the longer travel path by increasing the extrusion rate. This theory proved to be right, where it was discovered that the internal systems were increasing the extrusion rate in linear fashion according to the traveled path. After implementation of correcting coefficient into the G-code, printer was able to print a layer with good resolution and without visible over extrusion, which in quick succession led to our first successful honeycomb design. This scaffold was designated as Honeycomb 1.0 (Fig. 16a). It retained all the properties of the original Honeycomb design generated

using PrusaSlicer software with one difference. When a sample is being created following PrusaSlicer design, individual layers are beings stacked on top of each other with a rotation of 60°, whereas our iterations place layers without any rotation, meaning that every layer faces the same direction. Design was later used to create two more honeycomb infill structures with emphasis on maintaining porosity, which proved to be more of a geometrical problem. However, after a quick optimalization and a few tested iterations, we achieved three functioning designs showcased in Fig. 16 Following iterations were designated as “Honeycomb 1.5” (Fig. 16b) and “Honeycomb 2.0” (Fig. 16c), where the numbers 1.5 and 2.0 refer to size multiplication of internal honeycomb units. These were then successfully printed and tested.

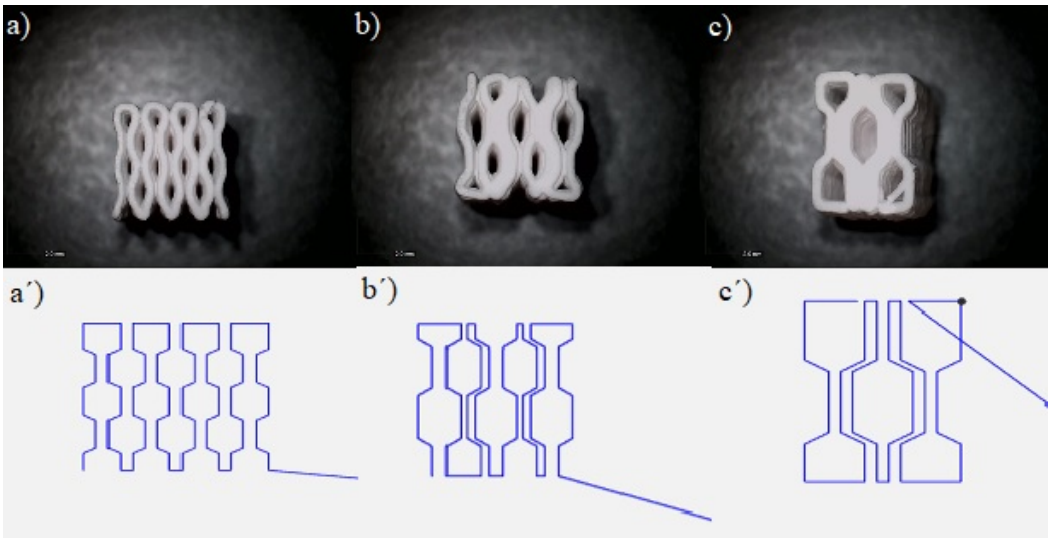

***Fig. 16**: Top view comparison of designed G-code and its subsequent successful print. a), a´) 1.0x iteration with 50% porosity; b), b´) 1.5x increased pore size; c), c´) 2.0x increased pore size*

4.3.1 Designed mold for non-porous samples

All the samples in this thesis are designed and then printed porous. As was mentioned before there are many beneficial reasons for their inherent porosity, but in terms of mechanical properties, porosity brings many variables into the equation. Subsequently, determining mechanical properties like strength or modulus of elasticity in our porous samples, we can’t talk about mechanical properties of the material, rather mechanical properties of each sample. To determine and establish reference in terms of strength of our CPC material, non-porous samples with the same dimensions had to be created and tested. For this purpose, positive of a mold was design and printed on Zmorph VX FAB 3D printer station rebuild to its original configuration using FDM method depositing molten PLA filament. The finished mold was then cast with silicone, which after curing formed the final mold for non-porous samples.

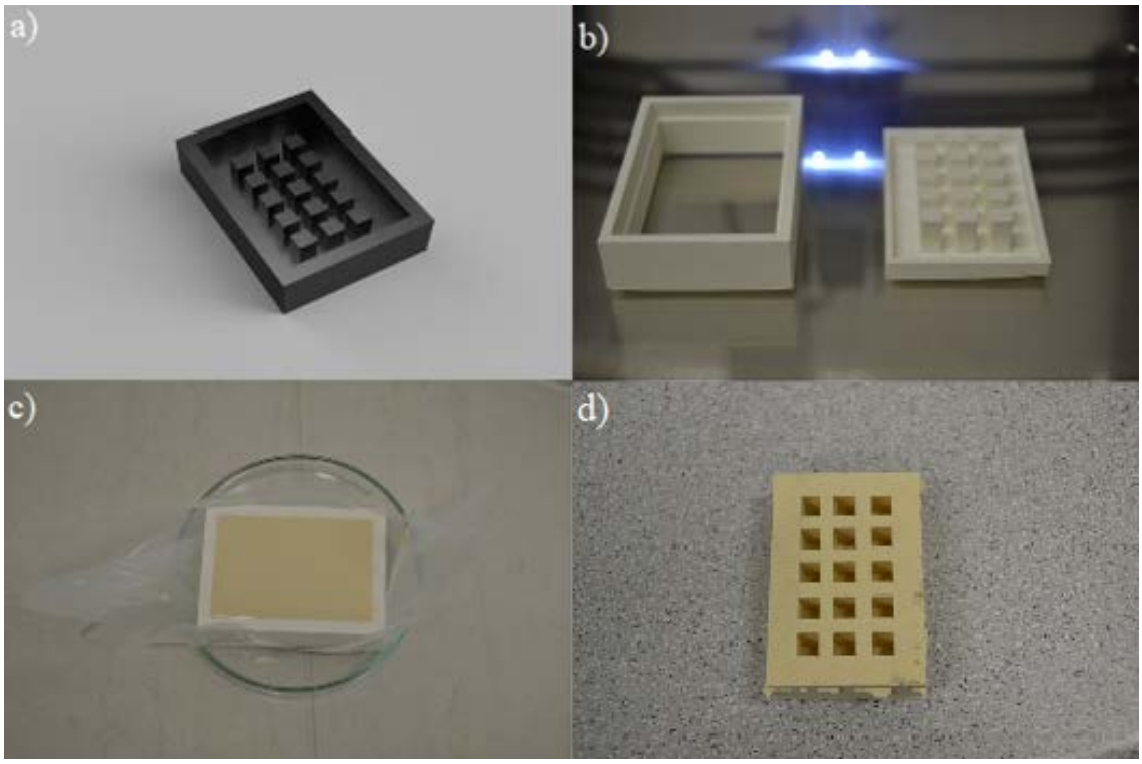

Fig. 17*: Mold for non-porous 6x6x12 mm rectangular samples: a) 3D design of the mold; b) 3D printed PLA positive of a mold; c) mold casted with silicone; d) final silicone mold*

4.4 Determination of mechanical properties

In this chapter, mechanical properties of designed structures will be discussed. The following properties were determined: strength; elastic gradient; absorbed energy. All measured values are listed in Table B.1 in appendix B. The measured deformation curves for each structure are listed in Appendix A. From these were subsequently selected individual deformation curves representing non-abnormal behavior shown in Fig 18.
Six internal structures and one referential were tested. From the six various structures three were of our own honeycomb design and three were default infill structures designed by the PrusaSlicer software. Last sample tested was a solid block with no internal porosity meant as a reference to establish the mechanical properties of used CPC paste. All tested iterations are showcased in Fig. 19.

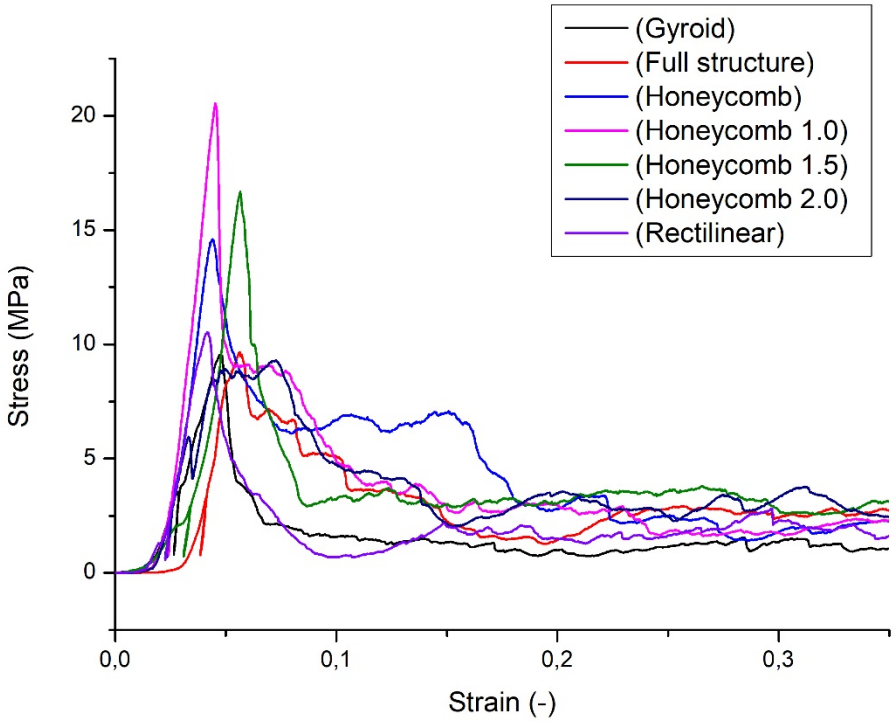

Fig. 18: *Selected deformation curves of tested structures*

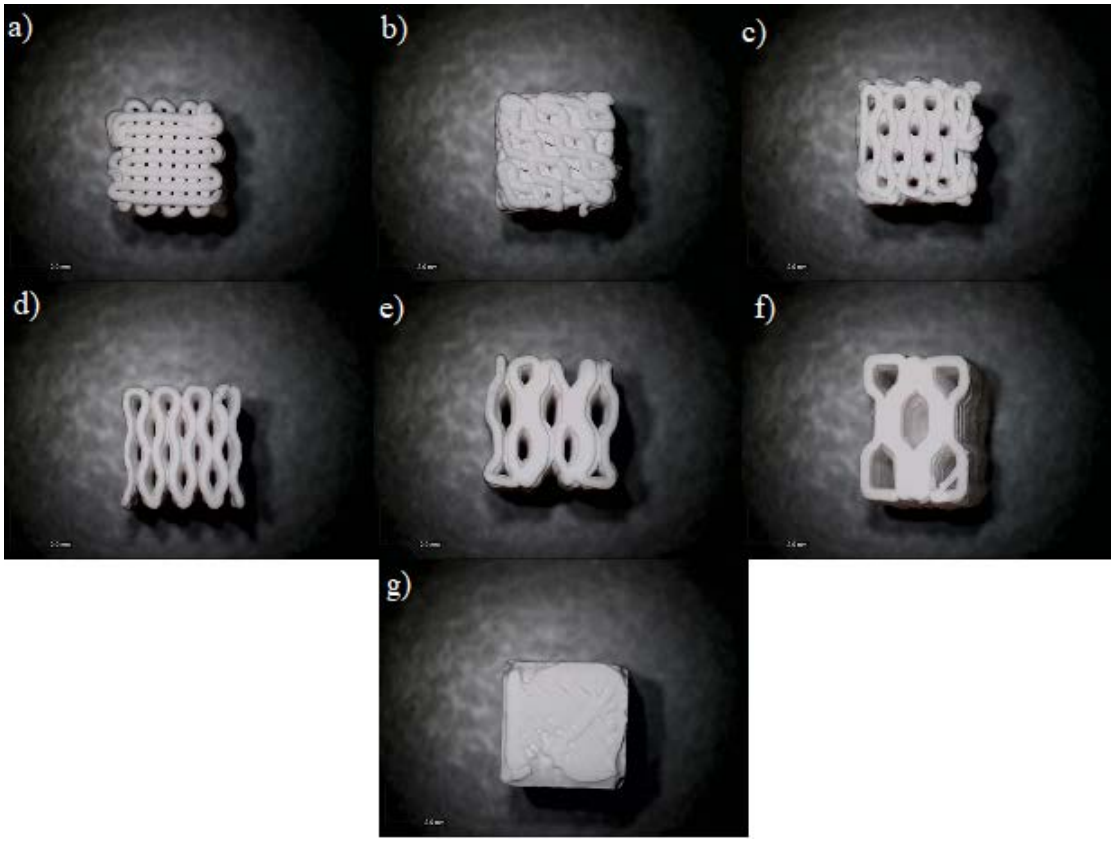

Fig. 19: *Showcase of all used internal structures: a) rectilinear; b) gyroid; c) Honeycomb; d) Honeycomb 1.0x; e) Honeycomb 1.5x; f) Honeycomb 2.0x; g) full structures*

In order to check the printing quality, photos were taken using a Microscope Leica TL3000, showcased in Fig 20 and Fig 21. Filament widths were subsequently measured on the observed structures, which confirmed good printing quality and filament width reproducibility. The images show reclinear and gyroid structures, with the rectilinear observing the quality of filaments in structures with a straight path of the printer head, and the gyroid structure observing the quality of filaments after more complicated paths were introduced. In both cases, filaments achieved reproducible results with the average width of filaments around 500 µm. The use of SEM would be necessary for more precise results.

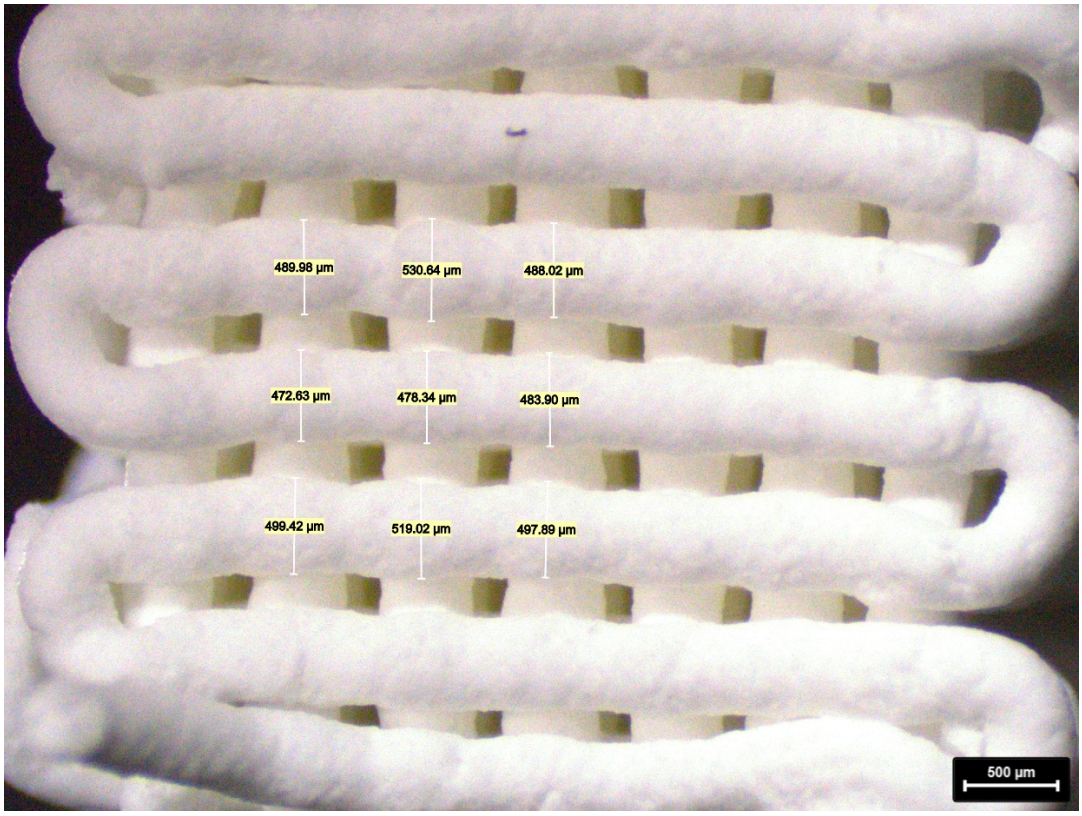

Fig. 19: *Measured filaments of rectlinear structure after hardening*

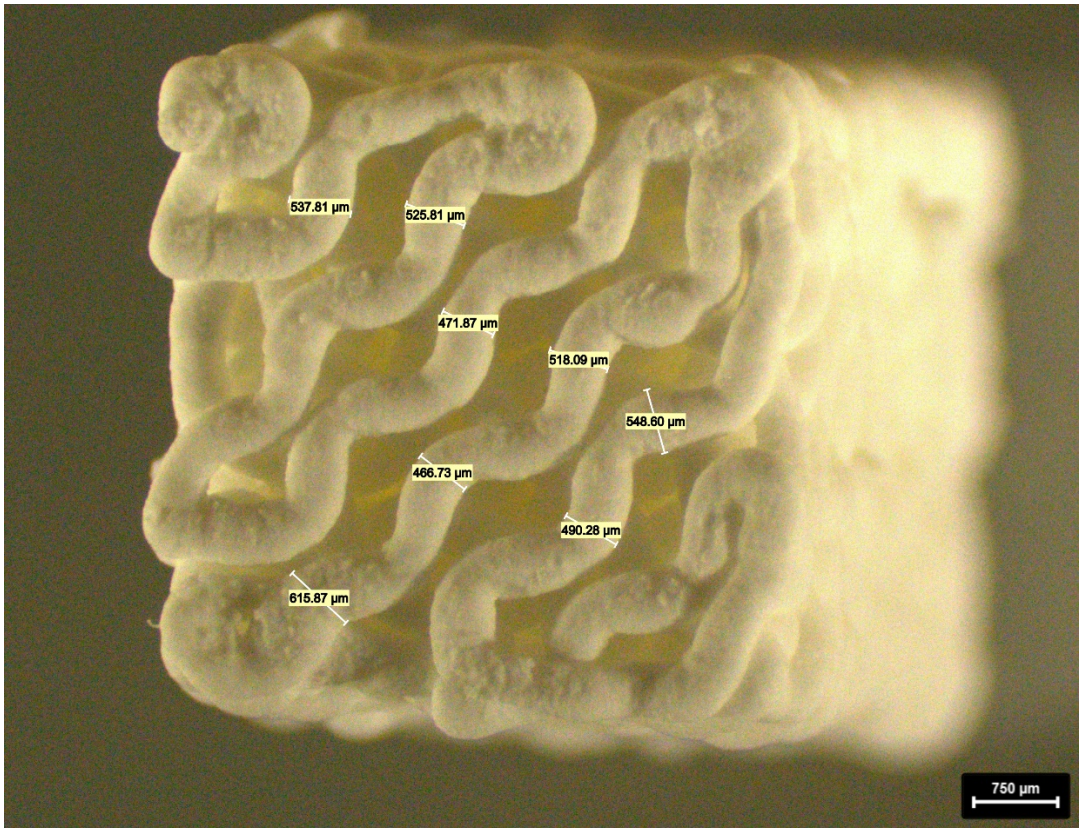

Fig. 20: *Measured filaments of gyroid structure after hardening*

4.4.1 Compressive strength

The results of compressive strength are shown in Fig. 26 showcased in box plot chart, together with statistical analysis showcasing statistically significant results connected and marked by a *. When observing the data, it is necessary to mention that they are all subject to a relatively high standard deviation even after using a high number of test samples. Highest values were achieved by samples with Honeycomb 1.0 internal structure, with median compressive strength of 16 MPa. Very similar results were reached by original Honeycomb and Honeycomb 1.5 internal structures, which achieved median compressive strength of 13.4 MPa for Honeycomb and 14.9 MPa for Honeycomb 1.5. After considering the standard deviations, all the above-mentioned internal structures show very similar compressive strengths. Honeycomb 2.0 reached lower values of median compressive strength at 8.6 MPa. Gyroid and rectilinear structure reached median values of 7.1 and 8.2 MPa.

When we look at our reference of non-porous sample, it achieved median value of 8.6 MPa, 96% lower than the highest value achieved by Honeycomb 1.0. There are few possible explanations for the occurrence of this phenomenon. First possible theory was that the smaller strength was caused by incomplete conversion of α-TCP to CDHA during the curing process. The samples had to be cured in silicone mold, which did not allow them to be removed before the samples cured. For this reason, only the top of the sample was exposed to moisture. In addition, even if the samples could be removed from the mold, their non-porous structure would not allow such moisture penetration as in the porous structure of other samples which could lead to the small conversion. However, acquired data of Elastic gradient, which will be discussed later, suggested very similar material properties, which would mean similar conversions in all tested samples. To verify said theory, X-ray diffraction analysis (XRD) was performed, shown in Fig. 27, which shows three measurements: (α-TCP) before conversion, porous sample after hardening for three days, full structure hardening for three days. We can see that in (α-TCP) before conversion highest peaks were at 30.7° proving high contents of (α-TCP). Consequently, in both porous infill structures and full structures, are curves very similar showing highest peaks at 31,72° specific for CDHA crystal. The conversion calculation further showed that in both cases there was recorded a high average conversion namely 81.6% for non-porous samples and 81.7% in porous samples. Average values for conversion of porous samples were supplied by David Scholz. These findings refuted the original theory of low conversion rate and prompted a new approach to solve the problem. Silicone mold could have affected full structure samples in other way, specifically it is possible that the casting mold confined the samples volumetrically, hindering the formation of CDHA crystals, which are responsible for strength in the material. However, this would require SEM analysis of crystalline structure to either confirm or refute said theory, which, unfortunately, is not possible in the scope of this work and should be explored further in future research.

Another possible theory deals with the dissipation of stress in observed structures. Under applied force, material has the tendency to flex in opposite direction which creates stress centers in non-porous internal structures, whereas porous structures allow the material to flex and expand into the pore without creating additional stress centers. This leads to better stress distribution in porous structures compared to non-porous ones, which could explain the significant difference in their performance.

When we start to compare the performance of our porous structures, honeycomb infill proved to have the highest strength with all the used honeycomb designs except Honeycomb 2.0, achieving almost 96% higher values. The observed trend can be explained by the strand architecture in different scaffolds. Where gyroid and rectilinear scaffolds are built with layers being placed on each other with rotation after each layer, our honeycomb designs place layers on each other in the same direction with no rotation. This leads to formulation of longitudinal pillars with tubular like walls aligned in the direction of applied load. On the other hand, in gyroid or rectilinear scaffolds shifting layers overlap much less, leading to creation of reduced vertical pillars, resulting in lower compressive strengths [92, 93, 94]. Furthermore, honeycomb internal structures (expect Honeycomb 2.0) exhibited an interesting destruction behavior where during the process of mechanical testing, samples were fractured in a way that they created conical debris. Such behavior was perceived in other studies [95], suggesting that failure patterns follow contact faces. In such failures, friction between the plates can be perceived, appearing as shear stress possible attributing to higher strength of honeycomb structures. Observed destruction behaviors are showcased in Figures 21. 22. 23. and 24.

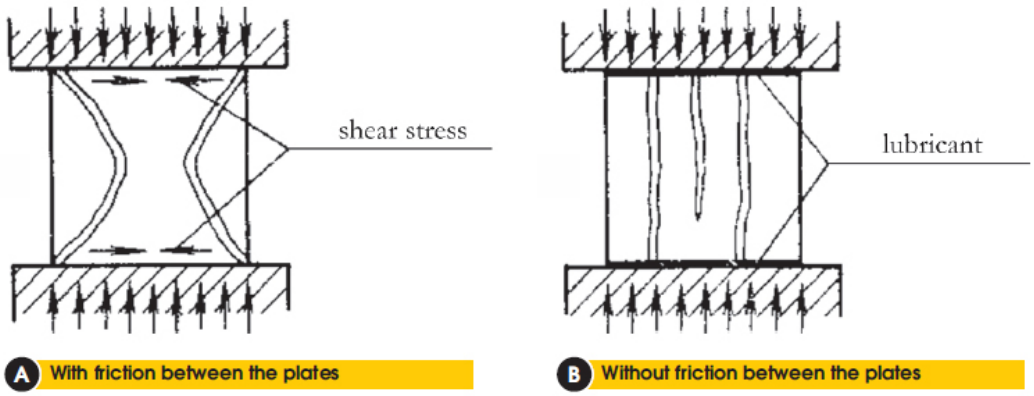

Fig. 21: *Failure modes perceived in cubical specimens [95]*

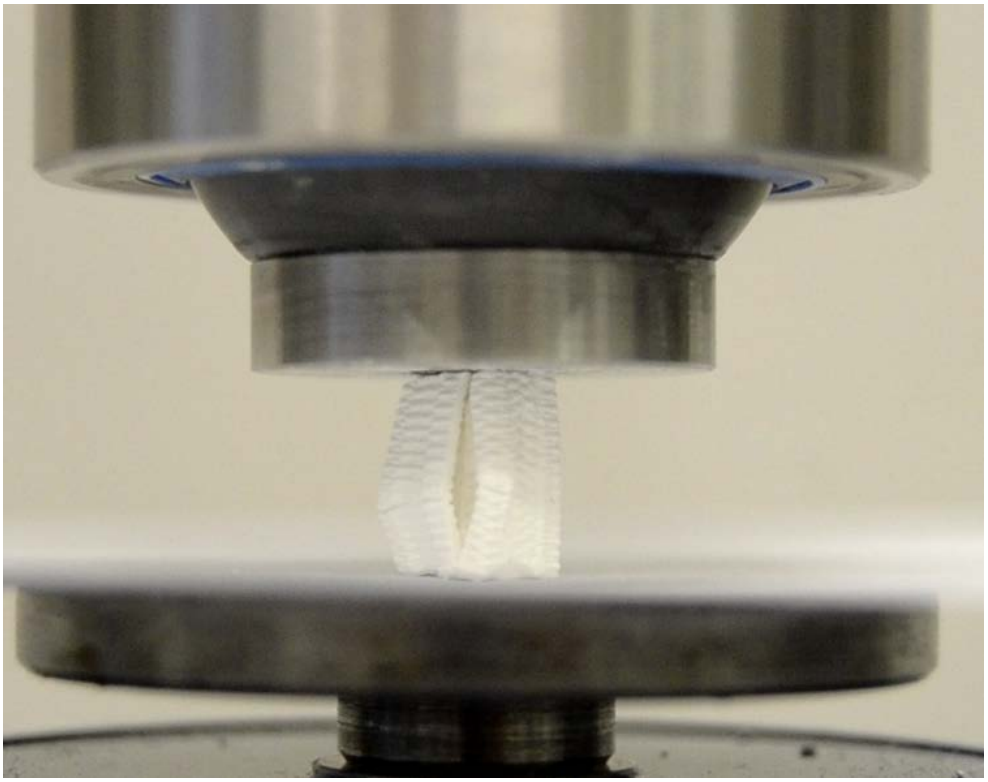

Fig. 22: *Destruction of Honeycomb structure with friction between the plates*

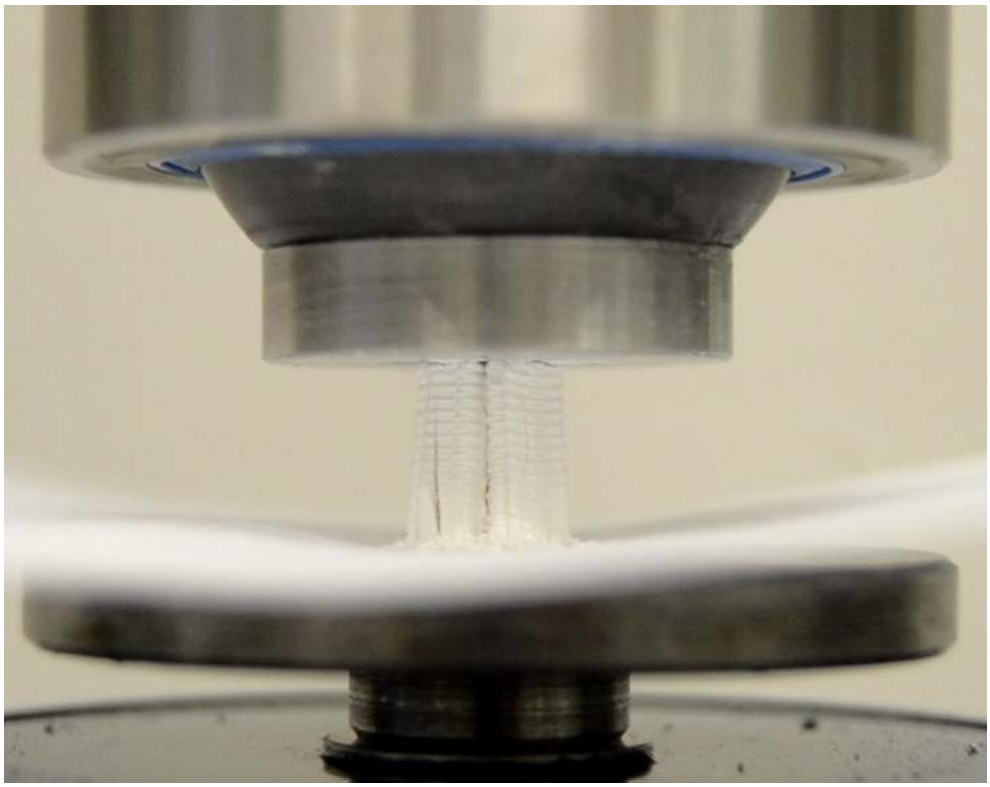

Fig. 23: *Destruction of Honeycomb 1.5 structure without friction between the plates*

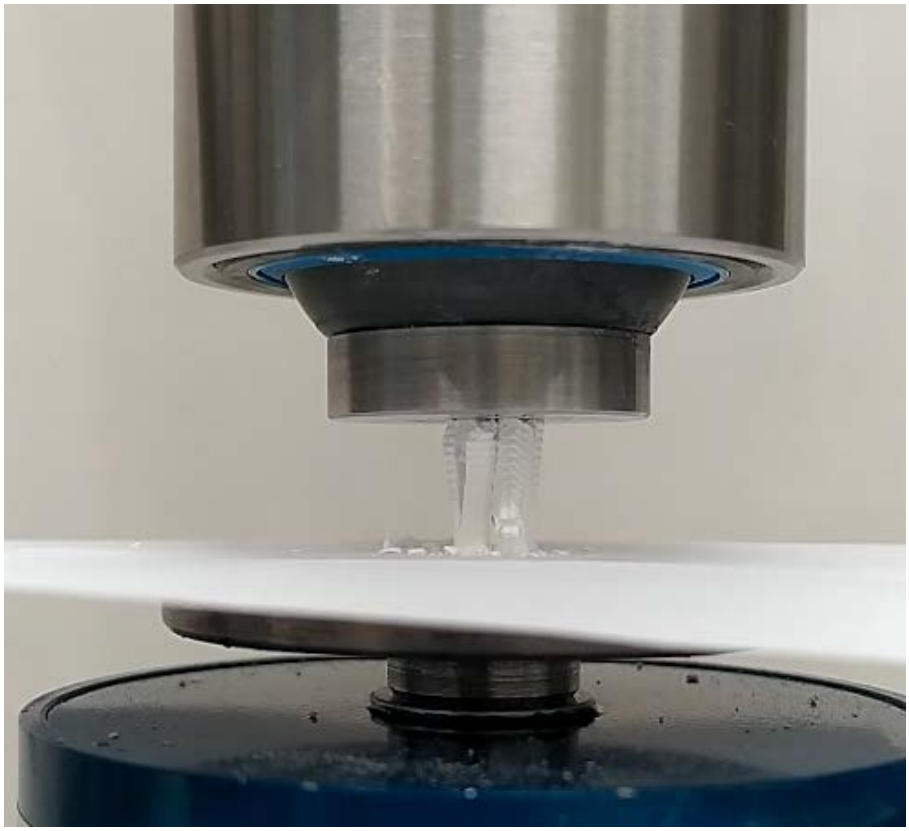

Fig. 24: *Destruction of Honeycomb 1.0 structure with friction between the plates*

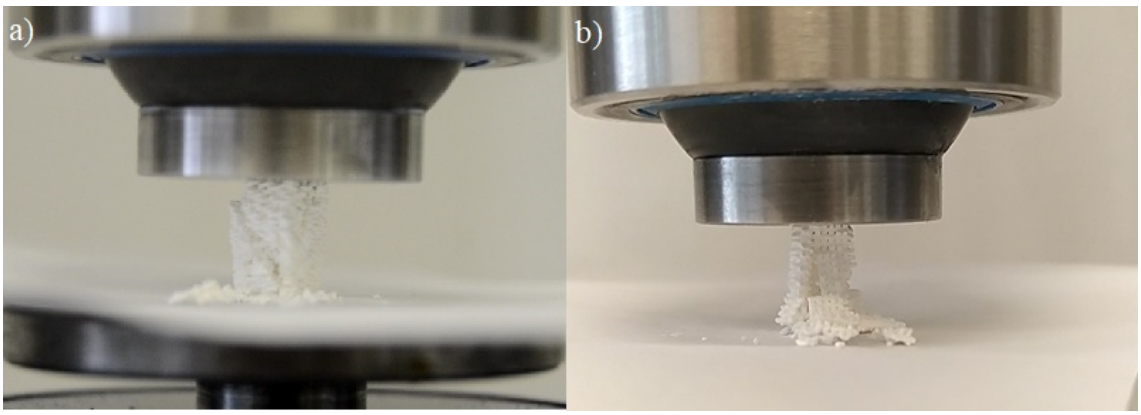

Fig. 25*: Destruction of a) Gyroid and rectilinear structures b) without friction between plates*

Another possible factor for higher performance of our designs is the fact, that they were created and manufactured in one go without breaking the filament. PrusaSlicer is optimized to select the fastest possible print head path when creating a scaffold structure, but this leads to fiber tearing with quick changes of printhead position. The fibers thus torn can then act as stress concentration centers which than compromise the structural integrity**.**

Some studies suggested no correlation between compressive strength and

macroporosity [92]. Even though, all the designed scaffolds aimed for porosity of 50 %, designs like Honeycomb 2.0 achieved targeted porosity by integrating large internal cells. These subsequently had an obvious effect on the resulting strength.

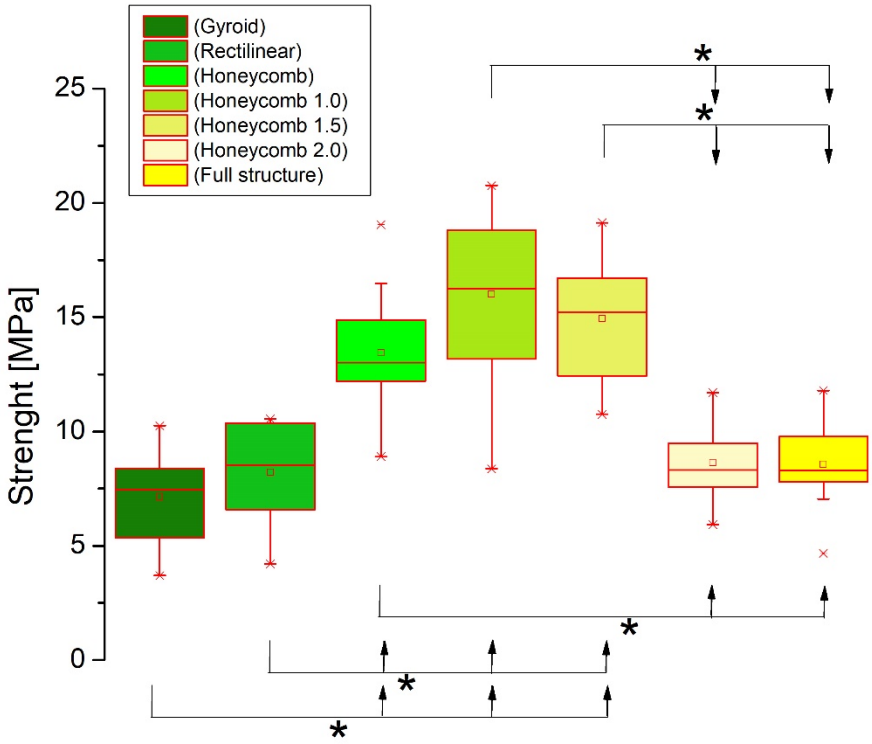

Fig. 26: *Compressive strength achieved by different infill structures. Statistically significant results are connected and marked by **

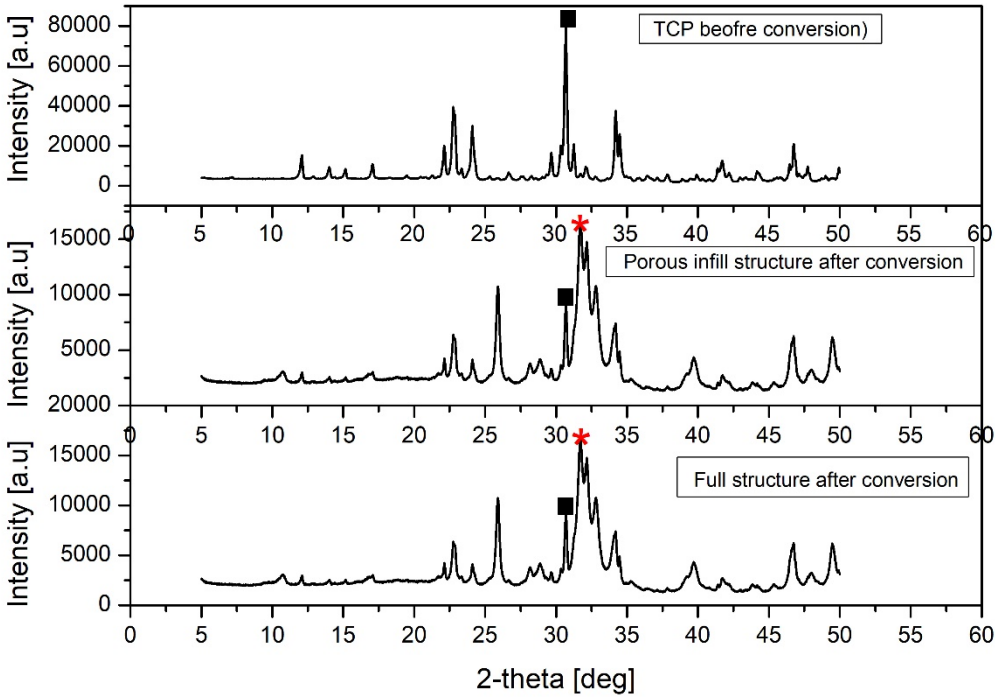

Fig. 27: *XRD diagrams of: a) (α-TCP) before conversion showcasing highest peak at 30.74 marked by cube;b) porous infill structure showcasing small intensity of (α TCP) at 30.7° (marked by cube) and higher peak of CDHA at 31.72°(marked by red star star); c) full structure showcasing small intensity of (α TCP) at 30.7° (marked by cube) and higher peak of CDHA at 31.72°(marked by red star star);*

4.4.2 Elastic gradient

Results of elastic gradient are showcased in Fig. 28. At first glance, we can see that the individual scaffolds were achieving approximately similar values of elastic gradient, even thou they are subjected to relatively high standard deviations. Highest value was achieved once again by Honeycomb 1.0, at median of 1178.1 MPa and lowest value by rectilinear scaffold at median of 935.4 MPa. Reference value of full structure was at median of 951.1 MPa which can be considered as the value of the elastic gradient of our CPC material. This statement is supported by the similar value of the elastic gradient for all scaffolds used, where we can see that the elastic gradient is more property of the material than a property of the structure.

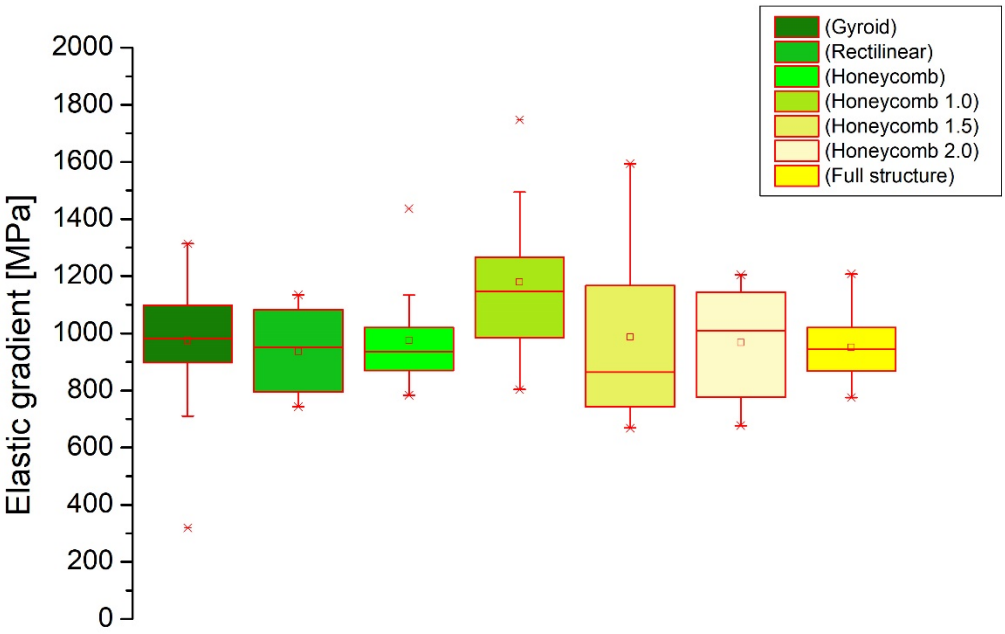

Fig. 28: *Elastic gradient of used internal structures in CPCs scaffold*

4.4.3 Absorbed energy

Measured values for absorbed energy are showcased in Fig. 29, together with statistical analysis showcasing statistically significant results connected together and marked by a *. The highest value was achieved by iteration of Honeycomb 1.5 scaffold. at median of 2.17 $MJ.m^{-3}$. The lowest value was achieved by the gyroid scaffold at median of 0.61 $MJ.m^{-3}$. Once again, all the recorded values are subjected to a relatively high standard deviation, but a clear trend can be perceived. Scaffolds designed by PrusaSlicer software, Gyroid and Rectilinear, achieved lesser values of absorbed energy at median of 0.61 $MJ.m^{-3}$ for Gyroid and 0.62 $MJ.m^{-3}$ for Rectilinear scaffold. At the same time, these designs proved to be subjected to the highest standard deviations, indicating higher unreliability. On the other hand, all designed honeycomb scaffolds achieved relatively high values of absorbed energy, even when compared to reference Full structure scaffold which was in theory supposed to perform the best. This could be once again attributed to the formulation of tubular like walls aligned in the direction of applied force, well suited for absorbing energy. Reference sample achieved values of median 1.68 $MJ.m^{-3}$ with a narrow variance of values which could indicate real values of capability to absorb energy of the used CPC material.

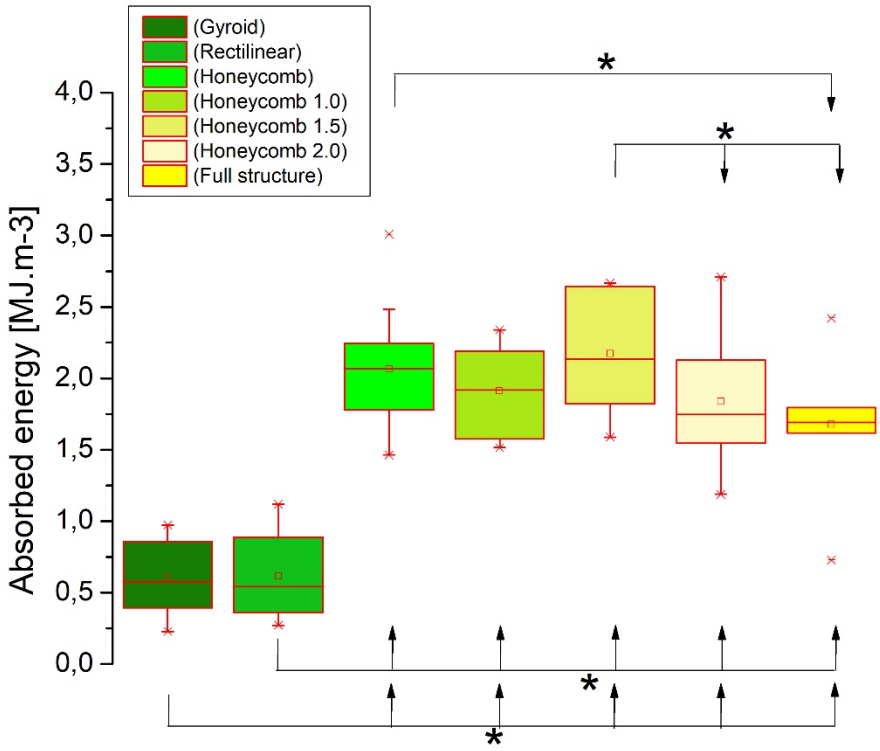

Fig. 29: *Absorbed energy of used internal structures in CPCs scaffolds. Statistically significant results are connected and marked by **

*

5. CONCLUSION

This diploma thesis dealt with the study of the effect of morphology on the mechanical properties of 3D printed bone scaffolds with the aim of designing and determining the best usable scaffold.

First, rigorous optimalization was conducted to secure reproducible and reliable results. This included optimalization of printing parameters like, printing speed, height of a first layer, extrusion coefficient.

After confirming reliable printable procedures, the ideal shape of printed samples was studied: cylindrical and cubic. Both shapes were printed with two infill structures, gyroid and rectilinear, and subjected to mechanical testing. Already at this point, it was possible to observe high standard deviations affecting results, which prompted us to choose the shape with more reliable results. This proved to be the cubic shape with repeating deformation curves and smaller standard deviations. The choice of cubic shape was later confirmed as right, when in the process of designing our scaffolds, it was possible to change the parameters of the infill structure in a way that the cylindrical shape would not allow.

When it came to designing customized infill structures, honeycomb was chosen as the template. Three designs were created: Honeycomb 1.0; Honeycomb 1.5; Honeycomb 2.0. All were successfully printed and consequently tested. To achieve successful results, fundamentals of used 3D printer must have been understood after which functional G-code could have been written. This opened possibilities to design and customize many more infill structures which could prove to have superior mechanical properties and further advance the bone cement scaffolds and offer opportunities for future research.

Seven different structures were tested for mechanical properties. Three designed by PrusaSlicer software, three of our own design and one referential sample with no infill structure. In each, strength, elastic gradient and absorbed energy was determined. Overall, Honeycomb designs proved to be superior, where nearly all except Honeycomb 2.0 achieved statistically significant higher values in strength and in absorbed energy than other compared scaffolds. Highest value for strength achieved by Honeycomb 1.0 was 96% higher than average values achieved by other conventionally used infill structures. In the context of future designs of CPC scaffolds, it would be desirable to further study all possible factors influencing the excellent results of honeycomb structures, as it could prove to bring many benefits in terms of mechanical properties and further bring us closer to the properties of bone.

In conclusion, morphology has shown its great influence on the resulting mechanical properties, being able to nearly double the resulting strength of material. Understanding the process of 3D printing and its programing allows for nearly unlimited range of customization opening possibilities for superb bone substitutes.

6. LITERATURE

[1] ROSETI, Livia, et al. Scaffolds for bone tissue engineering: state of the art and new perspectives. Materials Science and Engineering: C, 2017, 78: 1246-1262.

[2] AGARWAL, Rachit; GARCÍA, Andrés J. Biomaterial strategies for engineering implants for enhanced osseointegration and bone repair. Advanced drug delivery reviews, 2015, 94: 53-62.

[3] BAUER, Thomas W.; SCHILS, Jean. The pathology of total joint arthroplasty. *Skeletal radiology*, 1999, 28.9: 483-497.

[4] GIANNOUDIS, Peter V., Haralambos DINOPOULOS a Eleftherios TSIRIDIS, 2005. Bone substitutes: An update. Injury. 36(3), S20-S27. ISSN 00201383. Dostupné z: doi:10.1016/j.injury.2005.07.029

[5] BOSE, Susmita, Sahar VAHABZADEH a Amit BANDYOPADHYAY, 2013. Bone tissue engineering using 3D printing: An update. Materials Today. 16(12), 496-504. ISSN 13697021. Dostupné z: doi:10.1016/j.mattod.2013.11.017

[6] WILLIAMS, David, Sahar VAHABZADEH a Amit BANDYOPADHYAY, 2004. Benefit and risk in tissue engineering: An update. Materials Today. 7(5), 24-29. ISSN 13697021. Dostupné z: doi:10.1016/S1369-7021(04)00232-9

[7] ZHANG, Xiang-Yu; FANG, Gang; ZHOU, Jie. Additively manufactured scaffolds for bone tissue engineering and the prediction of their mechanical behavior: A review. *Materials*, 2017, 10.1: 50.

[8] WEN, Yu, et al. 3D printed porous ceramic scaffolds for bone tissue engineering: a review. *Biomaterials science*, 2017, 5.9: 1690-1698.

[9] RAYMOND, Santiago, et al. Accelerated hardening of nanotextured 3D-plotted self-setting calcium phosphate inks. Acta biomaterialia, 2018, 75: 451-462.

[10] SEARS, Nick A., et al. A review of three-dimensional printing in tissue engineering. *Tissue Engineering Part B: Reviews*, 2016, 22.4: 298-310.

[11] LANZA, Robert, et al. (ed.). *Principles of tissue engineering*. Academic press, 2020.

[12] KHADEMHOSSEINI, Ali; LANGER, Robert. A decade of progress in tissue engineering. Nature protocols, 2016, 11.10: 1775-1781.

[13] JONES, Julian R.; HENCH, Larry L. Regeneration of trabecular bone using porous ceramics. *Current Opinion in Solid State and Materials Science*, 2003, 7.4-5: 301-307.

[14] LIU, Yuchun; LIM, Jing; TEOH, Swee-Hin. Development of clinically relevant scaffolds for vascularised bone tissue engineering. *Biotechnology advances*, 2013, 31.5: 688-705.

[15] ROSETI, Livia, et al. Scaffolds for bone tissue engineering: state of the art and new perspectives. *Materials Science and Engineering: C*, 2017, 78: 1246-1262.

[16] CAMBRIDGE, U. O. TLP Library Structure of bone and implant materials -

Mechanical properties of bone 2014
http://www.doitpoms.ac.uk/tlplib/bones/bone_mechanical.php
[17] KEAVENY, Tony M.; HAYES, Wilson C. Trabecular Bone. *Bone: A Treatise*, 1992, 7: 285.
[18] RITCHIE, Robert O.; BUEHLER, Markus J.; HANSMA, Paul. Plasticity and toughness in bone. 2009.
[19] RITCHIE, Robert O. The conflicts between strength and toughness. *Nature materials*, 2011, 10.11: 817-822
[20] THAVORNYUTIKARN, Boonlom, et al. Bone tissue engineering scaffolding: computer-aided scaffolding techniques. *Progress in biomaterials*, 2014, 3.2-4: 61-102.
[21] TURNER, Brian N.; STRONG, Robert; GOLD, Scott A. A review of melt extrusion additive manufacturing processes: I. Process design and modeling. *Rapid Prototyping Journal*, 2014.
[22] GUVENDIREN, Murat, et al. Designing biomaterials for 3D printing. *ACS biomaterials science & engineering*, 2016, 2.10: 1679-1693.
[23] SHIRAZI, Seyed Farid Seyed, et al. A review on powder-based additive manufacturing for tissue engineering: selective laser sintering and inkjet 3D printing. *Science and technology of advanced materials*, 2015.
[24] KRUTH, J.-P., et al. Binding mechanisms in selective laser sintering and selective laser melting. *Rapid prototyping journal*, 2005.
[25] YAP, Chor Yen, et al. Review of selective laser melting: Materials and applications. *Applied physics reviews*, 2015, 2.4: 041101.
[26] MAZZOLI, Alida. Selective laser sintering in biomedical engineering. *Medical & biological engineering & computing*, 2013, 51.3: 245-256
[27] TUMBLESTON, John R., et al. Continuous liquid interface production of 3D objects. *Science*, 2015, 347.6228: 1349-1352.
[28] BARRY, John JA, et al. In vitro study of hydroxyapatite-based photocurable polymer composites prepared by laser stereolithography and supercritical fluid extraction. *Acta biomaterialia*, 2008, 4.6: 1603-1610.
[29] BRUNELLO, Giulia, et al. Powder-based 3D printing for bone tissue engineering. *Biotechnology advances*, 2016, 34.5: 740-753.
[30] DERBY, Brian. Inkjet printing of functional and structural materials: fluid property requirements, feature stability, and resolution. *Annual Review of Materials Research*, 2010, 40: 395-414.
[31] YOO, Hansol; KIM, Chongyoup. Experimental studies on formation, spreading and drying of inkjet drop of colloidal suspensions. *Colloids and Surfaces A: Physicochemical and Engineering Aspects*, 2015, 468: 234-245.
[32] BHARDWAJ, Rajneesh, et al. Self-assembly of colloidal particles from evaporating droplets: role of DLVO interactions and proposition of a phase diagram. *Langmuir*, 2010, 26.11: 7833-7842.

[33] ALI, Muhammad, et al. Controlling laser-induced jet formation for bioprinting mesenchymal stem cells with high viability and high resolution. *Biofabrication*, 2014, 6.4: 045001.

[34] DERAKHSHANFAR, Soroosh, et al. 3D bioprinting for biomedical devices and tissue engineering: A review of recent trends and advances. *Bioactive materials*, 2018, 3.2: 144-156.

[35] BILLIET, Thomas, et al. The 3D printing of gelatin methacrylamide cell-laden tissue-engineered constructs with high cell viability. *Biomaterials*, 2014, 35.1: 49-62.

[36] MOTA, Carlos, et al. Additive manufacturing techniques for the production of tissue engineering constructs. *Journal of tissue engineering and regenerative medicine*, 2015, 9.3: 174-190.

[37] Billiet, Thomas, et al. "The 3D printing of gelatin methacrylamide cell-laden tissue-engineered constructs with high cell viability." *Biomaterials* 35.1 (2014): 49-62.

[38] PELTOLA, Sanna M., et al. A review of rapid prototyping techniques for tissue engineering purposes. *Annals of medicine*, 2008, 40.4: 268-280.

[39] MAAZOUZ, Yassine, et al. Robocasting of biomimetic hydroxyapatite scaffolds using self-setting inks. *Journal of Materials Chemistry B*, 2014, 2.33: 5378-5386.

[40] CAO, Wanpeng; HENCH, Larry L. Bioactive materials. *Ceramics international*, 1996, 22.6: 493-507.

[41] SAMAVEDI, Satyavrata; WHITTINGTON, Abby R.; GOLDSTEIN, Aaron S. Calcium phosphate ceramics in bone tissue engineering: a review of properties and their influence on cell behavior. *Acta biomaterialia*, 2013, 9.9: 8037-8045.

[42] DOROZHKIN, Sergey V. Calcium orthophosphates: occurrence, properties, biomineralization, pathological calcification and biomimetic applications. *Biomatter*, 2011, 1.2: 121-164.

[43] BOHNER, Marc. Resorbable biomaterials as bone graft substitutes. *Materials Today*, 2010, 13.1-2: 24-30.

[44] NILEN, R. W. N.; RICHTER, P. W. The thermal stability of hydroxyapatite in biphasic calcium phosphate ceramics. *Journal of Materials Science: Materials in Medicine*, 2008, 19.4: 1693-1702.

[45] RAFFY MIRZAYAN, M. D.; MENENDEZ, Lawrence R. A Comparison of Mineral Bone Graft Substitutes for Bone Defects.

[46] CARRODEGUAS, Raúl G.; DE AZA, Salvador. α-Tricalcium phosphate: Synthesis, properties and biomedical applications. *Acta biomaterialia*, 2011, 7.10: 3536-3546.

[47] KOLMAS, Joanna, et al. Alpha-tricalcium phosphate synthesized by two different routes: Structural and spectroscopic characterization. *Ceramics international*, 2015, 41.4: 5727-5733.

[48] KJALARSDÓTTIR, Lilja, Arna DÝRFJÖRD, Atli DAGBJARTSSON, et al. Bone remodeling effect of a chitosan and calcium phosphate-based composite. *Regenerative biomaterials*. Oxford University Press, 2019, **6**(4), 241-247 [cit. 2022-03-13]. ISSN 2056-3418. Dostupné z: doi:10.1093/rb/rbz009

[49] GINEBRA, Maria-pau, José-angel DELGADO, Ingela HARR, Amisel ALMIRALL, Sergio DEL VALLE a Josep A PLANELL. Factors affecting the structure and properties of an injectable self-setting calcium phosphate foam. *Journal of Biomedical Materials Research Part A*. Hoboken: Wiley Subscription Services, Inc., A Wiley Company, 2007, **80A**(2), 351-361. ISSN 1097-4636. Dostupné z: doi:10.1002/jbm.a.30886

[50] PEREZ, Roman A, Hae-won KIM a Maria-pau GINEBRA. Polymeric additives to enhance the functional properties of calcium phosphate cements. Journal of tissue engineering. London, England: SAGE Publications, 2012, 3(1), 2041731412439555-2041731412439555. ISSN 2041-7314. Dostupné z: doi:10.1177/2041731412439555

[51] COSTA-PINTO, Ana Rita, Rui L REIS a Nuno M NEVES. Scaffolds Based Bone Tissue Engineering: The Role of Chitosan. *Tissue engineering. Part B, Reviews* [online]. United States: Mary Ann Liebert, 2011, **17**(5), 331-347

[52] XU, Hockin H.K., Shozo TAKAGI, Limin SUN, Latiff HUSSAIN, Laurence C. CHOW, William F. GUTHRIE a James H. YEN, 2006. Development of a nonrigid, durable calcium phosphate cement for use in periodontal bone repair. *The Journal of the American Dental Association*. **137**(8), 1131-1138. ISSN 00028177. Dostupné z: doi:10.14219/jada.archive.2006.0353

[53] VOJTOVA, Lucy, et al. The effect of the thermosensitive biodegradable PLGA–PEG–PLGA copolymer on the rheological, structural and mechanical properties of thixotropic self-hardening tricalcium phosphate cement. *International journal of molecular sciences*, 2019, 20.2: 391.

[54] QIAO, Mingxi, et al. Injectable biodegradable temperature-responsive PLGA–PEG–PLGA copolymers: synthesis and effect of copolymer composition on the drug release from the copolymer-based hydrogels. *International journal of pharmaceutics*, 2005, 294.1-2: 103-112.

[55] CHAMRADOVÁ, I., et al. The effect of hydroxyapatite particle size on viscoelastic properties and calcium release from a thermosensitive triblock copolymer. *Colloid and Polymer Science*, 2017, 295.1: 107-115.

[56] PEREZ, Roman A.; MESTRES, Gemma. Role of pore size and morphology in musculo-skeletal tissue regeneration. *Materials Science and Engineering: C*, 2016, 61: 922-939.

[57] PILLIAR, R. M.; LEE, J. M.; MANIATOPOULOS, C. D. D. S. Observations on the effect of movement on bone ingrowth into porous-surfaced implants. *Clinical orthopaedics and related research*, 1986, 208: 108-113.

[58] LEE, Sang Jin, et al. Macroporous biodegradable natural/synthetic hybrid scaffolds as small intestine submucosa impregnated poly (D, L-lactide-co-glycolide) for tissue-engineered bone. *Journal of Biomaterials Science, Polymer Edition*, 2004, 15.8: 1003-1017.

[59] BAKSH, D.; DAVIES, J. E.; KIM, S. Three-dimensional matrices of calcium polyphosphates support bone growth in vitro and in vivo. *Journal of materials science: Materials in medicine*, 1998, 9.12: 743-748.

[60] HULBERT, SFea, et al. Potential of ceramic materials as permanently implantable skeletal prostheses. *Journal of biomedical materials research*, 1970, 4.3: 433-456.

[61] KARAGEORGIOU, Vassilis; KAPLAN, David. Porosity of 3D biomaterial scaffolds and osteogenesis. *Biomaterials*, 2005, 26.27: 5474-5491.

[62] ROOSA, Sara M. Mantila, et al. The pore size of polycaprolactone scaffolds has limited influence on bone regeneration in an in vivo model. *Journal of Biomedical Materials Research Part A: An Official Journal of The Society for Biomaterials, The Japanese Society for Biomaterials, and The Australian Society for Biomaterials and the Korean Society for Biomaterials*, 2010, 92.1: 359-368.

[63] MURPHY, Ciara M.; HAUGH, Matthew G.; O'BRIEN, Fergal J. The effect of mean pore size on cell attachment, proliferation and migration in collagen–glycosaminoglycan scaffolds for bone tissue engineering. *Biomaterials*, 2010, 31.3: 461-466.

[64] GARIBOLDI, Maria Isabella; BEST, Serena M. Effect of ceramic scaffold architectural parameters on biological response. *Frontiers in bioengineering and biotechnology*, 2015, 3: 151.

[65] HABIBOVIC, Pamela, et al. 3D microenvironment as essential element for osteoinduction by biomaterials. *Biomaterials*, 2005, 26.17: 3565-3575.

[66] HING, K. A., et al. Microporosity enhances bioactivity of synthetic bone graft substitutes. *Journal of Materials Science: Materials in Medicine*, 2005, 16.5: 467-475.

[67] ANNAZ, Basil, et al. Porosity variation in hydroxyapatite and osteoblast morphology: a scanning electron microscopy study. *Journal of Microscopy*, 2004, 215.1: 100-110.

[68] DELIGIANNI, Despina D., et al. Effect of surface roughness of hydroxyapatite on human bone marrow cell adhesion, proliferation, differentiation and detachment strength. *Biomaterials*, 2000, 22.1: 87-96.

[69] RUMPLER, Monika, et al. The effect of geometry on three-dimensional tissue growth. *Journal of the Royal Society Interface*, 2008, 5.27: 1173-1180.

[70] NELSON, Celeste M., et al. Emergent patterns of growth controlled by multicellular form and mechanics. *Proceedings of the National Academy of Sciences*, 2005, 102.33: 11594-11599.

[71] ARABNEJAD, Sajad, et al. High-strength porous biomaterials for bone replacement: A strategy to assess the interplay between cell morphology, mechanical properties, bone ingrowth and manufacturing constraints. *Acta biomaterialia*, 2016, 30: 345-356.

[72] AFSHAR, M., et al. Additive manufacturing and mechanical characterization of graded porosity scaffolds designed based on triply periodic minimal surface architectures. *Journal of the mechanical behavior of biomedical materials*, 2016, 62: 481-494.

[73] BOCCACCIO, Antonio, et al. Geometry design optimization of functionally graded scaffolds for bone tissue engineering: A mechanobiological approach. *PloS one*, 2016, 11.1: e0146935.

[74] HU, L. L.; ZHOU, M. Zh; DENG, H. Dynamic indentation of auxetic and non-auxetic honeycombs under large deformation. *Composite Structures*, 2019, 207: 323-330.

[75] BARTHELAT, F., et al. On the mechanics of mother-of-pearl: a key feature in the material hierarchical structure. *Journal of the Mechanics and Physics of Solids*, 2007, 55.2: 306-337.

[76] YANG, Li, et al. Modeling of uniaxial compression in a 3D periodic re-entrant lattice structure. *Journal of Materials Science*, 2013, 48.4: 1413-1422.

[77] JANG, Dongchan, et al. Fabrication and deformation of three-dimensional hollow ceramic nanostructures. *Nature materials*, 2013, 12.10: 893-898.

[78] LI, Sheng, et al. The development of TiNi-based negative Poisson's ratio structure using selective laser melting. *Acta Materialia*, 2016, 105: 75-83.

[79] ZHANG, Jianjun; LU, Guoxing; YOU, Zhong. Large deformation and energy absorption of additively manufactured auxetic materials and structures: A review. *Composites Part B: Engineering*, 2020, 108340.

[80] XIAO, Dengbao, et al. Insight into the negative Poisson's ratio effect of metallic auxetic reentrant honeycomb under dynamic compression. *Materials Science and Engineering: A*, 2019, 763: 138151.

[81] VIJAYAVENKATARAMAN, Sanjairaj; GOPINATH, Akhil; LU, Wen F. A new design of 3D-printed orthopedic bone plates with auxetic structures to mitigate stress shielding and improve intra-operative bending. *Bio-Design and Manufacturing*, 2020, 3.2: 98-108.

[82] JIN, Yuan, et al. Fabrication of multi-scale and tunable auxetic scaffolds for tissue engineering. *Materials & Design*, 2021, 197: 109277.

[83] ABUEIDDA, Diab W., et al. Mechanical properties of 3D printed polymeric Gyroid cellular structures: Experimental and finite element study. *Materials & Design*, 2019, 165: 107597.

[84] GERMAIN, Loic, et al. 3D-printed biodegradable gyroid scaffolds for tissue engineering applications. *Materials & Design*, 2018, 151: 113-122.

[85] DOLAN, James A., et al. Optical properties of gyroid structured materials: from photonic crystals to metamaterials. *Advanced Optical Materials*, 2015, 3.1: 12-32.

[86] OLIVARES, Andy L., et al. Finite element study of scaffold architecture design and culture conditions for tissue engineering. *Biomaterials*, 2009, 30.30: 6142-6149.

[87] JUNG, Gang Seob; BUEHLER, Markus J. Multiscale mechanics of triply periodic minimal surfaces of three-dimensional graphene foams. *Nano letters*, 2018, 18.8: 4845-4853.

[88] MA, Shuai, et al. Mechanical behaviours and mass transport properties of bone-mimicking scaffolds consisted of gyroid structures manufactured using selective laser melting. *Journal of the mechanical behavior of biomedical materials*, 2019, 93: 158-169.

[89] SCHERER, Maik Rudolf Johann. *Double-Gyroid-Structured functional materials: synthesis and applications*. Springer Science & Business Media, 2013.

[90] RAJAGOPALAN, Srinivasan; ROBB, Richard A. Schwarz meets Schwann: design and fabrication of biomorphic and durataxic tissue engineering scaffolds. *Medical image analysis*, 2006, 10.5: 693-712.

[91] MICHLOVSKÁ, Lenka, Lucy VOJTOVÁ, Ludmila MRAVCOVÁ, Soňa HERMANOVÁ, Jiří KUČERÍK and Josef JANČÁŘ. Functionalization Conditions of PLGA-PEG-PLGA Copolymer with Itaconic Anhydride. Macromolecular Symposia. 2010, 295(1), 119-124. DOI: 10.1002/masy.200900071. ISSN 10221360. Available from: http://doi.wiley.com/10.1002/masy.200900071

[92] RAYMOND, Santiago, et al. Accelerated hardening of nanotextured 3D-plotted self-setting calcium phosphate inks. *Acta biomaterialia*, 2018, 75: 451-462.

[93] MIRANDA, Pedro, et al. Mechanical properties of calcium phosphate scaffolds fabricated by robocasting. *Journal of Biomedical Materials Research Part A: An Official Journal of The Society for Biomaterials, The Japanese Society for Biomaterials, and The Australian Society for Biomaterials and the Korean Society for Biomaterials*, 2008, 85.1: 218-227.

[94] MAAZOUZ, Yassine, et al. Robocasting of biomimetic hydroxyapatite scaffolds using self-setting inks. *Journal of Materials Chemistry B*, 2014, 2.33: 5378-5386.

[95] BEZERRA, Ulisses Targino, et al. Hourglass-shaped specimen: compressive strength of concrete and mortar (numerical and experimental analyses). *Revista Ibracon de Estruturas e materiais*, 2016, 9.4: 510-524.

7. ABBREVIATIONS

Abbreviations:

ABA	PLGA-PEG-PLGA
AM	additive manufacturing
AFM	atomic force microscopy
ACP	amorphous calcium phosphates
BTS	bone tissue engineering
CAD	computer-aided design
Ca/P	calcium phosphates
CDHA	calcium-deficient hydroxyapatite
CIJ	continuous inkjet printing
CPC	ceramics calcium phosphate cement
CT	computer tomography
DCP	anhydrous dicalcium phosphate
DCPD	dicalcium phosphate dihydrate
DIW	direct ink writing
DOD	drop-on-demand inkjet printing
FDM	Fused deposition modeling
HA	hydroxyapatite
L/P	liquid/powder
MRI	magnetic resonance imagining
OCP	octocalcium phosphate
PB	particle binding
PLGA- PEG- PLGA	Poly(D,L-lactic acid-co-glycolic acid)-b-poly(ethylene glycol) b-poly(D,L-lactic acid-co-glycolic acid) triblock copolymer
SEM	scanning electron microscopy
SLA	stereolithography
SLS	selective laser sintering
β-TCP, α-TCP	β- and α- tricalcium phosphates
TPMS	triply periodic minimal surfaces
XRD	X-ray powder diffraction

8. FIGURES

9. TABLES

Appendix A - Figures

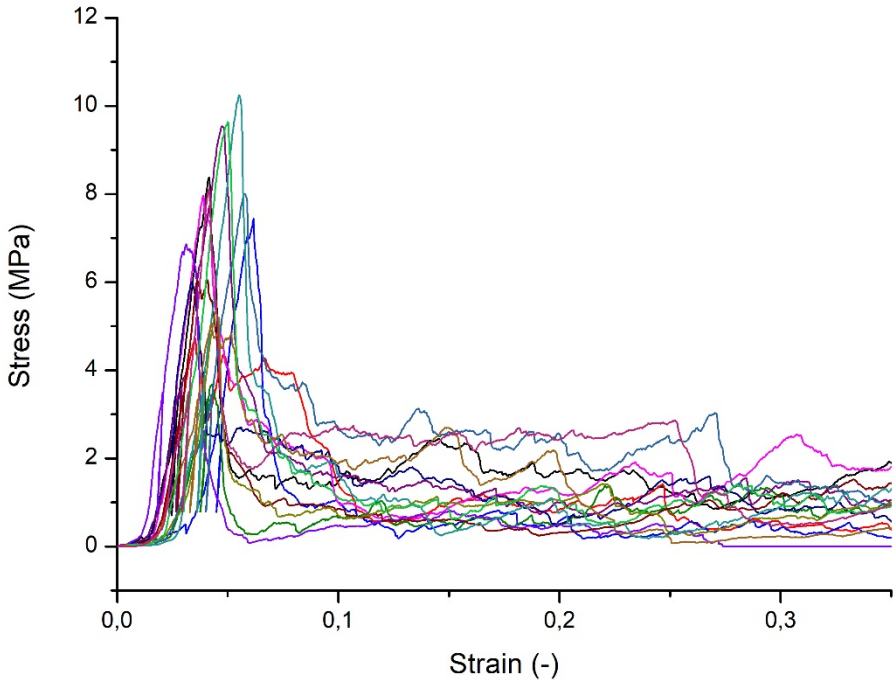

Fig. A.1: *Deformation curves of measured samples gyroid infill structure*

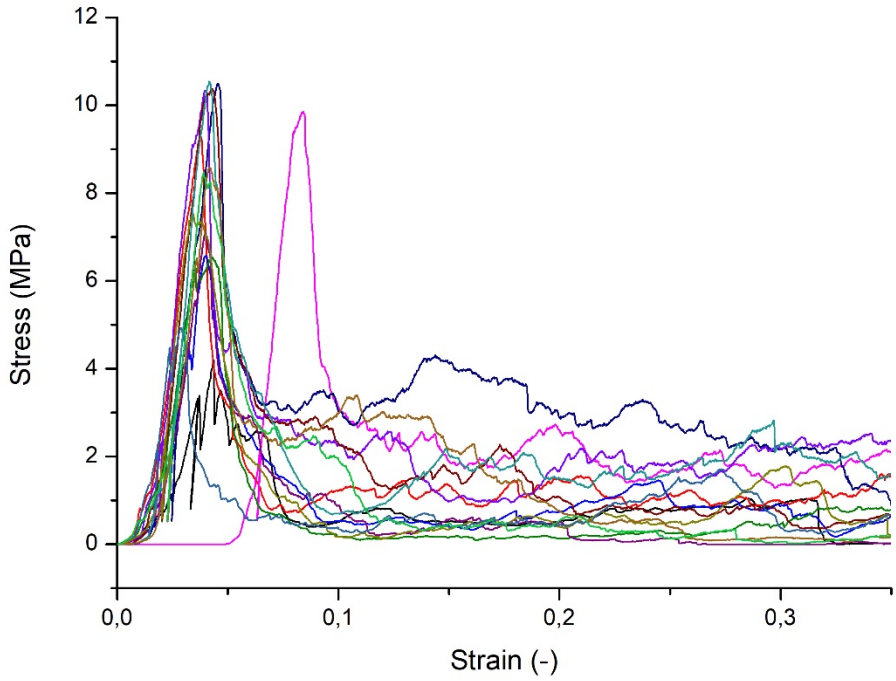

Fig. A.2: *Deformation curves of measured samples rectilinear infill structure*

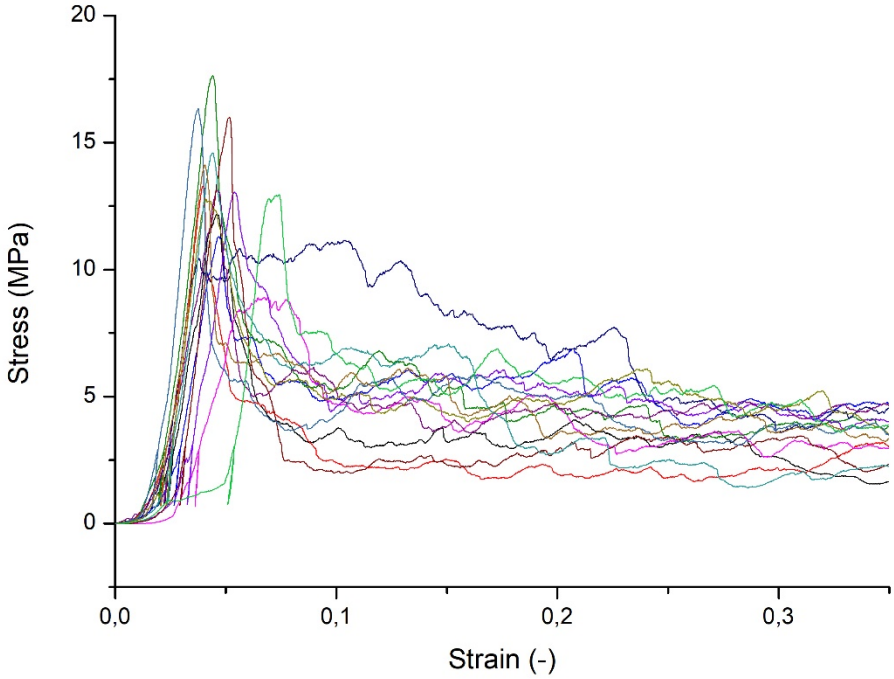

Fig. A.3: *Deformation curves of measured samples Honeycomb infill structure*

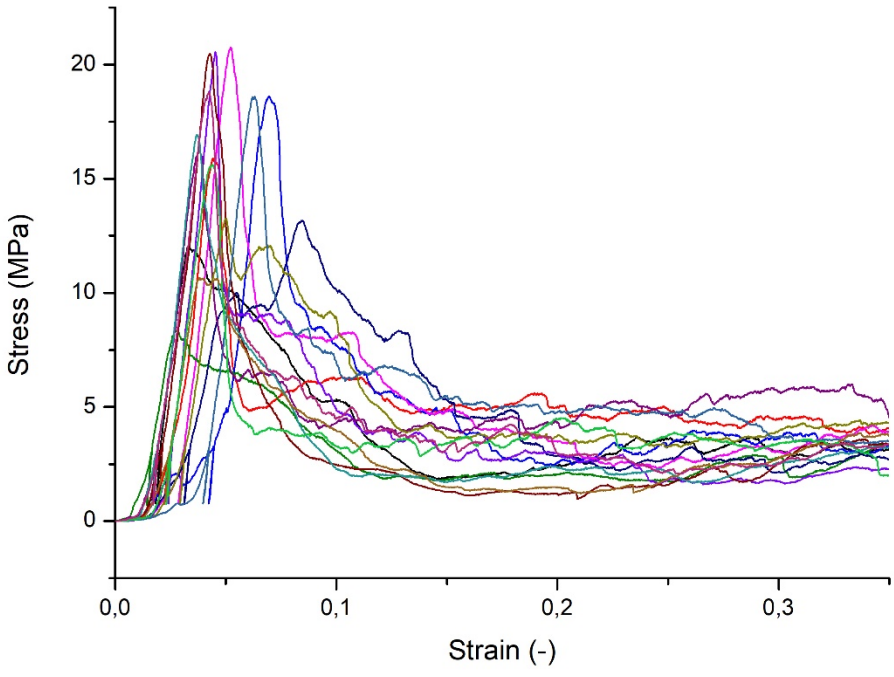

Fig. A.4: *Deformation curves of measured samples Honeycomb 1.0 infill structure*

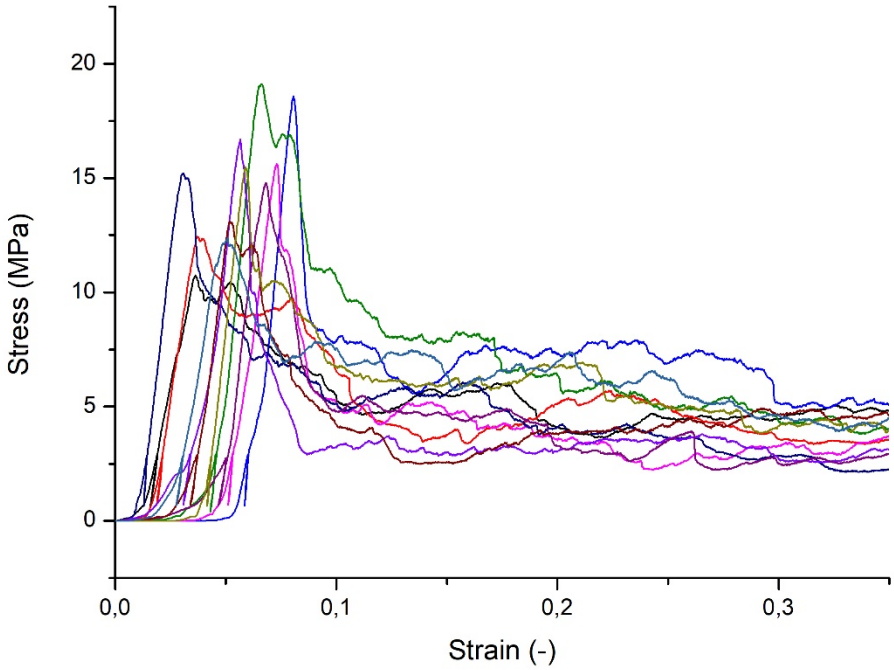

Fig. A.5: *Deformation curves of measured samples Honeycomb 1.5 infill structure*

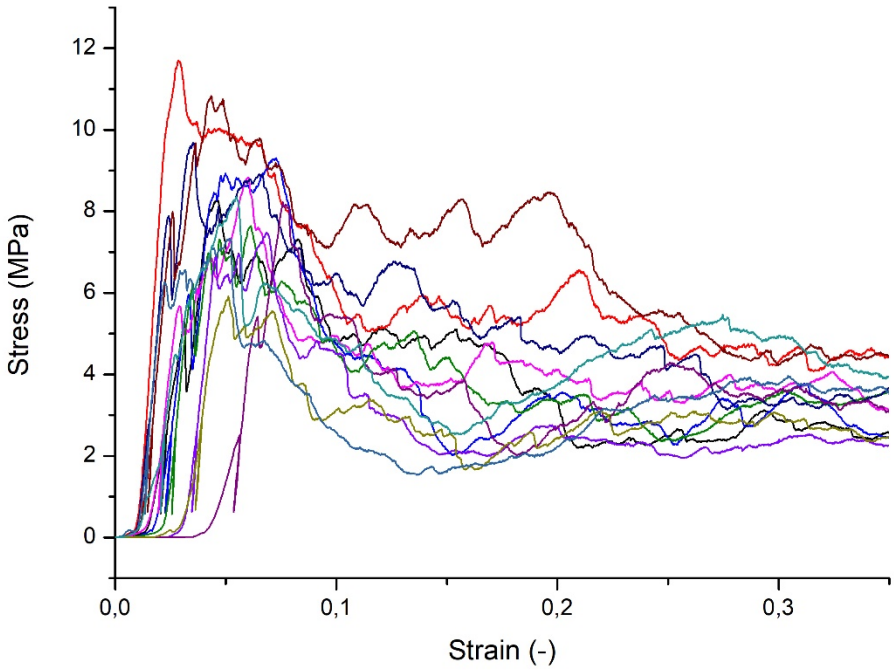

Fig. A.6: *Deformation curves of measured samples Honeycomb 2.0 infill structure*

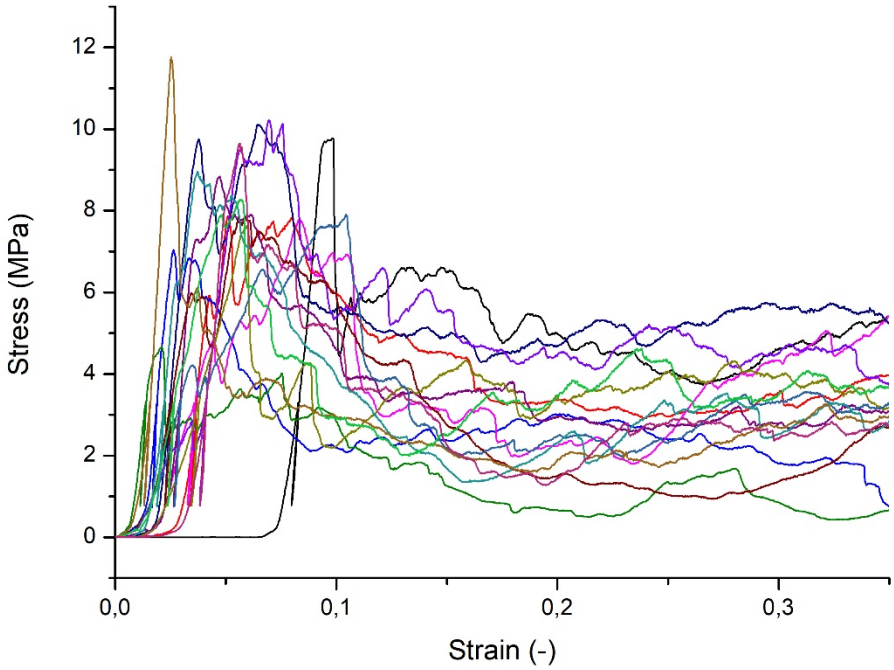

Fig. A.7: *Deformation curves of measured samples full infill structure*

Appendix B – Tables

Table B1: *Measured average values of mechanical observed mechanical properties*

	Strength [MPa]	**Elastic gradient [MPa]**	**Absorbed energy [MJ.m^{-3}]**
Gyroid	7.1	975.1	0.61
Rectilinear	8.2	935.4	0.62
Honeycomb	13.4	974.5	2.06
Honeycomb 1.0	16	1178.1	1.91
Honeycomb 1.5	14.9	986.1	2.17
Honeycomb 2.0	8.6	967.2	1.84
Full structure	8.6	951.1	1.68